Development of L-Band Down Converter Boards and

Real-time Digital Backend for Phased Array Feeds

Vikas Asthana

A thesis submitted to the faculty of
Brigham Young University
in partial fulfillment of the requirements for the degree of

Master of Science

Karl F. Warnick, Chair
Brian D. Jeffs
David G. Long

Department of Electrical and Computer Engineering

Brigham Young University

June 2012

ABSTRACT

Development of L-Band Down Converter Boards and
Real-time Digital Backend for Phased Array Feeds

Vikas Asthana
Department of Electrical and Computer Engineering
Master of Science

Recent developments in the field of phased array feeds for radio astronomical reflector antennas, have opened a new frontier for array signal processing for radio astronomy observations. The goal is to replace single horn feeds with a phased array feed, so as to enable astronomers to cover more sky area in less time. The development of digital backend signal processing systems has been a major area of concentration for the development of science-ready phased array feeds for radio astronomers.

This thesis focuses on the development of analog down-converter receivers and an FPGA-based digital backend for real-time data processing and analysis support for phased array feeds. Experiments were conducted with new receiver boards and both single-polarization and dual-polarization phased array feeds at the Arecibo Observatory, Puerto Rico and at the 20-meter telescope at Green Bank, WV, and results were analyzed. The experiments were performed as a part of a feasibility study for phased array feeds.

The new receiver boards were developed as an upgrade to the earlier connectorized receivers as the number of input channels increased from 19 to 38 and space constraints arose due to the large size of the earlier receivers. Each receiver card has four independent channels on it. The receiver cards were found to have lower cross-coupling between the channels in comparison to the earlier receivers.

The development of a FPGA-based real time digital backend focused on a real-time spectrometer, beamformer and a correlator for all the 64-channels using a x64 ADC card and ROACH FPGA boards. The backend can plot results in real time and can stream and store the data on the computers for purpose of post-processing and data analysis. The design process uses libraries and blocks provided by the Center for Astronomy Signal Processing and Electronics Research (CASPER) community.

Keywords: phased array feeds, L-Band down converters, radio astronomy, signal processing

ACKNOWLEDGMENTS

Table of Contents

List of Tables

List of Figures

Chapter 1

Introduction

1.1   Radio Astronomy

Radio astronomy is the study of celestial objects in the universe that emit radio waves. Radio astronomy helps scientists to study astronomical phenomena that are often invisible in other portions of the electromagnetic spectrum. Typically, astronomical signals are extraordinarily weak since these signals travel through vast interstellar distances before reaching an observer on Earth. Detection of these weak astronomical signals has always been the goal for the radio telescopes from the early days of radio astronomy [2]. The main parameters for developing the radio astronomy instruments include more collecting area, lower noise floor and greater field of view. More collecting area allows us to observe known phenomena deeper and greater field of view opens the possibility of finding new phenomena such as transient radio sources and pulsars.

Traditional waveguide feed horn antennas cannot be packed tightly enough to provide a continuous image in one snapshot due to their physically large size. These feeds provide independent sky mapping pixels with low main beam overlap, making the reflector focal plane not fully sampled [3] [4]. Recent developments in the field of phased array feeds (PAFs) for radio astronomical reflector antennas, have opened a new frontier for array signal processing for radio astronomy observations.

PAFs consists of closely spaced electrically small elements. A PAF can be used as a "radio camera," to image a field of view several beamwidths in diameters, enabling rapid wide-field sky surveys and continuous sky coverage. PAFs have several advantages over traditional horn feeds, such as multiple steered beams, greater control over beam patterns and sensitivity optimization with respect to noise environment.

As astronomical signals are extremely weak, detection of such sources require high sensitivity, and higher gain stability for detection with long integration times. PAFs offer the potential

to achieve such high sensitivity by optimizing beam patterns to maximize the performance for a given type of observation. Radio telescopes like the Low Frequency Array (LOFAR) [5], the Allen Telescope Array (ATA) [6], the Square Kilometer Array (SKA) [7], the Green Bank Telescope (GBT) [8] and the Arecibo Radio Telescope [9] are making significant steps towards replacing the single horn feed antennas with the PAFs. This will help them perform in a better way by enhancing their capabilities, and the scientists and astronomers will be able to complete their experiments and observations at a higher rate.

The various organizations spread all over the world are currently working on the development of the PAFs. The Netherlands Foundation for Research in Astronomy (ASTRON) is working on project for multi-beam synthesis using an array of Vivaldi antennas for multi-beam synthesis [10]. The Canberra Deep Space Communication Complex (CDSCC), a part of Commonwealth Scientific and Industrial Research Organization (CSIRO), Australia, is working on building a new dish with a phased array feed and multiple channel data acquisition system [11]. China has started construction of the Five hundred meter Aperture Spherical Telescope (FAST), the world's largest single-aperture radio telescope and is considering PAFs as a major antenna system for the installation [12].

A lot of effort has also been put been in developing the instrumentation and the back-ends for the feeds installed on the radio telescopes. This involves design of receivers, down-converters, A/D converters and the back-ends to store the data on the computers for post-processing. There has been a focus on making the back-ends capable of doing correlator and beamforming in real-time. The Collaboration for Astronomical Signal Processing and Electronics Research (CASPER) at the University of California, Berkeley has become a global community with collaboration from other universities involved in developing the new instrumentation designs. The goal of the community is to simplify the design of radio astronomy instruments by developing reusable designs using platform-independent, open-source hardware and software [13].

1.2   Thesis Contributions

This thesis provides the details about the recent backend hardware development for use with the PAFs. The first contribution is the design and characterization of an analog down-converter receiver board, which was built as an upgrade to the earlier connectorized down-converter receiver

boxes. The need to upgrade arose due to the increased number of channels and space constraints for the whole system setup for experiments. Each receiver board has four channels expanding the system to 40 channels from 20 channels within a constrained space and the IF filter is placed on the board itself, which earlier required a different setup and a power supply of its own. Cross coupling between the channels on same board and between the boards has been reduced by a significant amount in comparison to the receiver boxes.

Another contribution of this thesis is the analysis done for a feasibility study for the design of PAFs for the Arecibo observatory and the weak source imaging analysis done with observation data sets obtained from experiments at Arecibo and Green Bank, WV. This thesis documents the results obtained and setup done for the study of PAFs on Arecibo telescope and the 20m telescope at Green Bank for a series of experiments done over several months. It also discuss the digital backend requirements for the PAFs. The results discuss the field of view available, sensitivity of the PAFs over the entire aperture and the detection of weak astronomical sources using PAFs. It also discusses the analysis done for the weak source detection and variation in the noise field around the source using the data obtained from experiments at Green Bank.

A final contribution is the demonstration and development of a new real-time digital backend for our collaborators at the National Radio Astronomy Observatory (NRAO) and the University of Massachusetts (UMass). This documents the development of the digital backend for a millimeter wave PAF. It discusses different architectures and design requirements necessary for building such a system. The final goal of developing this backend is to replace the current data acquisition system with this real-time data processing backend. This involves developing a real-time 64-channel spectrometer, correlator and a beamformer.

1.3 Thesis Outline

The outline of the thesis is as follows:

Chapter 2, *Array Theory*, gives a background to basic array theory and beamforming algorithms. It also discusses the need and necessity of real-time digital backend for any instrument or feed built for the radio telescopes.

Chapter 3, *The Analog Down-Converters*, covers the design and characterization of the receivers boards designed for use with the PAFs. It also includes details about all the important components used to construct the receivers. Initial test results of the boards are also discussed.

Chapter 4, *The Feasibility Study of Phased Array Feed*, covers the details about the feasibility study done for the design of the PAFs for the Arecibo Observatory, PR and the Green Bank, WV. It discusses the setup procedure and the results obtained from the experiments.

Chapter 5, *The Real-Time Digital Backend*, covers the design and development of a real-time digital backend for the PAFs. It discusses various design procedures and architectures of the digital backend system. It also provides details about the current status of the system and the future work associated with the development of a digital backend to be used with the PAFs.

Chapter 6, *Conclusions and Future Work*, summarizes the important points of this thesis and provides suggestions for future research with the digital backend and the receivers for the PAFs.

Chapter 2

Array Theory

2.1 Antenna Model

An antenna can be modeled as an equivalent current distribution, which radiates the same field in a free space as compared to an antenna structure with a given excitation. The field radiated by such a current source can be calculated using a Green's function and a radiation integral.

For a given set of boundary conditions, a Green's function is the field radiated by a point or delta function source. For a point source in a homogeneous region, the electric field should satisfy the following partial differential equation,

$$[\nabla^2 + k^2]\bar{E}(\bar{r}) = j\omega\mu\bar{J}(\bar{r}). \tag{2.1}$$

To find a green's function, we have to solve for $\bar{E}$ for a point source of form

$$\bar{J}(\bar{r}) = \hat{p}\delta(\bar{r} - \bar{r}') \tag{2.2}$$

where $\bar{r}'$ is the location of the source and $\hat{p}$ is the polarization of the source.

While this equation (2.1) is easier to solve than Maxwell's equations, it provides non-physical solutions, but there exists an auxiliary potential which can give valid solutions. Using a theorem from differential geometry, it is found that the magnetic flux density $\bar{B}$ in Gauss's Law $\nabla \cdot \bar{B} = 0$, is the curl of some vector field, such that

$$\bar{B} = \nabla \times \bar{A} \tag{2.3}$$

where $\bar{A}$ is called the magnetic vector potential. Using this vector potential in Faraday's and Ampere's law leads to

$$[\nabla^2 + k^2]\bar{A} = -\mu\bar{J} + j\omega\mu\epsilon\nabla\phi + \nabla\nabla \cdot \bar{A}. \tag{2.4}$$

As there are many vector fields $\bar{A}$ that satisfy Eq.(2.3) for a given $\bar{B}$, we can choose a particular vector potential called Lorenz gauge, for which

$$\nabla \cdot \bar{A} = -j\omega\mu\epsilon\phi. \tag{2.5}$$

Using this in Eq.(2.4), the equation becomes

$$[\nabla^2 + k^2]\bar{A} = -\mu\bar{J}. \tag{2.6}$$

Now to solve Eq.(2.2) for a point source, $\bar{A}(\bar{r})$ is labeled as $g(\bar{r}, \bar{r}')$ for a point source located at $\bar{r}'$. For simplicity, the point source can be assumed to be located at origin, making $g(\bar{r}, \bar{r}') = g(r)$, thus the equation becomes

$$[\nabla^2 + k^2]g(r) = -\delta(\bar{r}). \tag{2.7}$$

Solving this and applying radiation boundary condition for outgoing waves, we get

$$g(r) = A\frac{e^{-jkr}}{r}. \tag{2.8}$$

Integrating left-hand side of Eq.(2.7) over a volume containing origin and equating to -1 to solve for A, we have $A = 1/4\pi$. Finding the final green function as a function of location $\bar{r}'$, we have the result as

$$g(r) = \frac{e^{-jk|\bar{r}-\bar{r}'|}}{4\pi |\bar{r} - \bar{r}'|}. \tag{2.9}$$

Now the radiation integral can be given as the integral of the scalar green's function weighted by the source distribution function $\bar{J}$,

$$\bar{A}(\bar{r}) = \mu \int g(\bar{r}, \bar{r}')\bar{J}(\bar{r}')d\bar{r}'. \tag{2.10}$$

The electric field can be found in terms of the magnetic vector potential as,

$$
\begin{aligned}
\bar{E} &= -j\omega\bar{A} - \nabla\phi \\
&= -j\omega\bar{A} + \frac{1}{j\omega\epsilon\mu}\nabla\nabla \cdot \bar{A} \\
&= -j\omega\left[1 + \frac{1}{k^2}\nabla\nabla \cdot\right]\bar{A}.
\end{aligned}
\tag{2.11}
$$

Putting the value of A from Eq.(2.10) in this Eq.(2.11), we have the radiation integral for electric field in free space as

$$
\bar{E} = -j\omega\mu\left[1 + \frac{1}{k^2}\nabla\nabla \cdot\right]\int g(\bar{r}, \bar{r}')\bar{J}(\bar{r}')d\bar{r}'.
\tag{2.12}
$$

The radiation integral can further be simplified by assuming the source to be near origin and the observation point far from the origin. This leads to following approximations

$$
|\bar{r} - \bar{r}'| = r - \hat{r} \cdot \bar{r}',
$$

$$
g(\bar{r}, \bar{r}') \simeq \frac{e^{-jkr}}{4\pi r}e^{jk\hat{r}\cdot\bar{r}'},
$$

$$
\text{and } \nabla \simeq -jk\hat{r}.
$$

These results reduce the radiation integral to

$$
\bar{E} = -j\omega\mu\left(1 - \hat{r}\hat{r} \cdot\right)\frac{e^{-jkr}}{4\pi r}\int e^{jk\hat{r}\cdot\bar{r}'}\bar{J}(\bar{r}')d\bar{r}'.
\tag{2.13}
$$

While solving this, it is easier to use spherical coordinates for $\bar{r}$ and rectangular coordinates for $\bar{r}'$, which resolve the expression $\hat{r} \cdot \bar{r}'$ as

$$
\hat{r} \cdot \bar{r}' = x'\sin\theta\cos\phi + y'\sin\theta\sin\phi + z'\cos\theta.
\tag{2.14}
$$

2.2 Antenna Parameters

2.2.1 Antenna Gain and Directivity

Directivity is a measure of how directional the radiation pattern of an antenna is in comparison to an isotropic antenna. The directivity D of an antenna is given by the ratio of radiated

7

power density in the given direction to the power density of an isotropic antenna radiating the same power. Hence the directivity is

$$D(\theta, \phi) = \frac{S_{\mathrm{av}}}{P_{\mathrm{rad}}/(4\pi r^2)} \tag{2.15}$$

where the total radiated power P_{rad} is given by

$$P_{\mathrm{rad}} = \oint_S \bar{S}_{\mathrm{av}} \cdot d\bar{S} \tag{2.16}$$

where S is a closed surface containing the antenna. The power density radiated by an isotropic antenna is given by

$$\bar{S}_{\mathrm{iso}} = \frac{P_{\mathrm{rad}}}{4\pi r^2}. \tag{2.17}$$

The directivity D is the maximum value of the directivity pattern. In terms of the effective area A_{eff} of an antenna, the directivity of an antenna is given by

$$D = A_{\mathrm{eff}} \frac{4\pi}{\lambda^2} \tag{2.18}$$

where λ is the wavelength of radiated energy. Multiplying D by the radiation efficiency gives the gain G of an antenna. The gain for a radio telescope can also be defined as the ratio of the antenna temperature T_{A} in Kelvin to the source flux density F_{s} in Jy, so that

$$G = \frac{T_{\mathrm{A}}}{F_{\mathrm{s}}} (\mathrm{K/Jy}). \tag{2.19}$$

2.2.2 Sensitivity

The sensitivity of the receiver is the performance measure of the smallest signal output from the system to get a minimum signal-to-noise ratio. The sensitivity of the system is limited by noise generated inside the system. In terms of antenna parameters, sensitivity can be given as

$$S = \frac{A_{\mathrm{eff}}}{T_{\mathrm{sys}}} \tag{2.20}$$

$$= \frac{\eta_{\mathrm{rad}}\eta_{\mathrm{ap}}A_{\mathrm{phy}}}{T_{\mathrm{sys}}} \tag{2.21}$$

8

where S is the sensitivity, A_{eff} is the effective area, T_{sys} is the system temperature, η_{rad} is the radiation efficiency and η_{ap} is the aperture efficiency. But since the actual physical area A_{phy} changes according to the dish, the sensitivity can be expressed as,

$$\frac{A_{\text{phy}}}{S} = \frac{T_{\text{sys}}}{\eta_{\text{rad}}\eta_{\text{ap}}} = \frac{T_{\text{sys}}}{\eta_{\text{ant}}} \tag{2.22}$$

where η_{ant} is the antenna efficiency.

2.2.3 Aperture Efficiency

From IEEE standards for antenna terms [14], the aperture efficiency of an antenna can be expressed as the ratio of the maximum directivity of an antenna to its standard directivity,

$$\eta_{\text{ap}} = \frac{D_0}{D_{\text{std}}} \tag{2.23}$$

where D_0 is the maximum directivity and D_{std} is the standard directivity which can also be expressed as,

$$D_{\text{max}} = \frac{4\pi}{\lambda^2} A_{\text{phy}} \tag{2.24}$$

where A_{phy} is the physical area of the dish.

2.3 Signal Model

For an array having N elements placed at the focus of the reflector of a dish, the voltage vector at the receiver chain outputs can be given as

$$\mathbf{v} = \mathbf{v}_{\text{s}} + \mathbf{v}_{\text{n}} \tag{2.25}$$

where the voltage vector $\mathbf{v}$,

$$\mathbf{v} = \begin{bmatrix} \mathbf{v}_1 \mathbf{v}_2 \cdots \mathbf{v}_{\text{N}} \end{bmatrix}^{\text{T}} \tag{2.26}$$

is the voltage matrix of all the N elements, and $\mathbf{v}_{\text{s}}$ denotes the signal voltage and $\mathbf{v}_{\text{n}}$ is the noise voltage. This noise voltage consist of contribution from large number of the noise sources, which

can be given as

$$\mathbf{v}_n = \mathbf{v}_{loss} + \mathbf{v}_{rec} + \mathbf{v}_{sky} + \mathbf{v}_{spill} \tag{2.27}$$

where $\mathbf{v}_{loss}$ is the voltage associated with the noisy components present in the system, $\mathbf{v}_{rec}$ is the voltage associated with the receiver chain, $\mathbf{v}_{sky}$ is the voltage associated with the noise from the sky and $\mathbf{v}_{spill}$ is the spillover noise associated with warm ground below the dish.

2.4 Correlation Matrix

Assuming all the components in Eq.(2.25) are independent, the correlation matrix can be found as

$$\mathbf{R}_t = E[\mathbf{v}\mathbf{v}^H] \tag{2.28}$$

$$= E[\mathbf{v}_{sig}\mathbf{v}_{sig}^H] + E[\mathbf{v}_{loss}\mathbf{v}_{loss}^H] + E[\mathbf{v}_{rec}\mathbf{v}_{rec}^H] + E[\mathbf{v}_{sky}\mathbf{v}_{sky}^H] + E[\mathbf{v}_{spill}\mathbf{v}_{spill}^H] \tag{2.29}$$

$$= \mathbf{R}_{sig} + \mathbf{R}_{loss} + \mathbf{R}_{rec} + \mathbf{R}_{sky} + \mathbf{R}_{spill} \tag{2.30}$$

$$= \mathbf{R}_{sig} + \mathbf{R}_{loss} + \mathbf{R}_{rec} + \mathbf{R}_{ext} \tag{2.31}$$

$$= \mathbf{R}_{sig} + \mathbf{R}_n \tag{2.32}$$

where $E[\cdot]$ denotes expectation, $\mathbf{R}_{sig}$ is the signal covariance matrix, $\mathbf{R}_{rec}$ is the receiver noise covariance matrix and $\mathbf{R}_{ext}$ is sum of the sky noise and spillover noise covariance matrix given by $\mathbf{R}_{sky}$ and $\mathbf{R}_{spill}$ respectively.

For our system usage, the information contained in this correlation matrix serves an input to calculate the beamformer weights and to form images of the sources.

2.5 Calibration

The use of PAFs on a radio telescope require calibration of these feeds. The PAFs can be calibrated by scanning the reflector on a near-bright astronomical source over a grid of pointings, and the voltage response from each array output channel is acquired. The noise output of the array is acquired by pointing the reflector to an "off" pointing, several degrees away from the bright source. This procedure provides array noise response to calculate the steering vectors, which can be used to form beams using a optimal beamforming algorithm [15].

The BYU PAF is calibrated by scanning the reflector over a near-bright source, such as Cassiopeia A (CasA) and the voltage responses from array output channels are stored in the form of an array correlation matrix for each grid pointing. This correlation matrix $\mathbf{R}_v$ is the sum of signal covariance matrix $\mathbf{R}_{\mathrm{sig}}$ and noise covariance matrix $\mathbf{R}_{\mathrm{n}}$,

$$\mathbf{R}_{\mathrm{v}} = E[\mathbf{v}\mathbf{v}^H] = \mathbf{R}_{\mathrm{sig}} + \mathbf{R}_{\mathrm{n}}. \tag{2.33}$$

The correlation matrix used is obtained by subtracting the noise correlation matrix $\mathbf{R}_{\mathrm{off}}^{\mathrm{c}}$ obtained from the off-pointing, from each of the on-pointing correlation matrix $\mathbf{R}_{\mathrm{on,n}}^{\mathrm{c}}$, where superscript c stands for the calibration data and n denotes the pointing index. It is given as

$$\mathbf{R}_{\mathrm{sig,n}} \simeq \mathbf{R}_{\mathrm{on,n}}^{\mathrm{c}} - \mathbf{R}_{\mathrm{off}}^{\mathrm{c}}. \tag{2.34}$$

2.5.1 Beamforming

Beamforming refers to a signal processing technique to steer the radiation pattern electronically or electrically, so as to cover more of the sky area and to increase the field of view [16]. The number of formed beams is directly proportional to the number of elements in an array. This is one of the major advantages of using the PAFs. The beamformer weights required to form a beam can be found by a variety of methods, one of the most commonly used is as discussed below.

2.5.2 Max SNR Beamformer

The signal-to-noise ratio for a signal is given by,

$$\mathrm{SNR} = \frac{\mathbf{w}^{\mathrm{H}}\mathbf{R}_{\mathrm{sig}}\mathbf{w}}{\mathbf{w}^{\mathrm{H}}\mathbf{R}_{\mathrm{n}}\mathbf{w}}. \tag{2.35}$$

Maximizing this with respect to $\mathbf{w}$ leads to a generalized eigenvalue equation of the form

$$\mathbf{R}_{\mathrm{n}}^{-1}\mathbf{R}_{\mathrm{sig}}\mathbf{w} = \left(\frac{\mathbf{w}^{\mathrm{H}}\mathbf{R}_{\mathrm{sig}}\mathbf{w}}{\mathbf{w}^{\mathrm{H}}\mathbf{R}_{\mathrm{n}}\mathbf{w}}\right)\mathbf{w}. \tag{2.36}$$

The principal eigenvector of Eq. (2.36) gives us the weight vector which maximizes the SNR. This solution obtained is called the Max SNR Beamformer. In practical, the steering vectors $\mathbf{V}_s$

are calculated over the grid points by taking out a significant eigenvector of the correlation matrix at each grid point, which is obtained from the solution of generalized eigenvalue equation of form,

$$\mathbf{R}_{\text{off}} \mathbf{w}_{\text{n}} = \lambda_{\text{max}} \mathbf{R}_{\text{on,n}} \mathbf{w}_{\text{n}}. \tag{2.37}$$

These steering vectors are then used to calculate the beamformer weights $\mathbf{w}$. Once the beamformer weights are obtained, they can be applied to the data from other sources to form images. The steering vectors are calculated from

$$\mathbf{w}_{\text{n}} = \mathbf{R}_{\text{n}}^{c-1} \mathbf{V}_{\text{s}}. \tag{2.38}$$

The normalization of these weight vectors may have to be done to make the correlation matrices similar with respect to the correlation matrices obtained from the other sources.

2.6   Necessity of Data Processing in Real-Time

The radio astronomer's research focuses on finding out the new phenomenons and objects in the sky. The main goal of the study is to discover more and more new sky area and to study the known phenomenons more deeply. For these, they perform various types of observations to observe the sky: on-off, extended source observation, spectral line observation, polarized sources observation and pulsar surveys. But there are many problems associated with these observations.

Most of these observations require a large amount of data processing. The data processing is a large time consuming process. The time consumed in processing increases directly with the number of elements present in the array. Also, this time consuming process make the astronomers lose some valuable science opportunities as they have to wait for the data to process. The data rate becomes too high with increasing array elements. There is a large amount of radio frequency interference (RFI) sources present in the atmosphere which gets mixed with the data, making it useless for the astronomer.

A real time data processing backend provide a solution to many of these problems. With real time data processing, the array feeds can be calibrated in real time and the weights can be calculated out for the formation of images and beamformers at the same time. Processing the data using high performance DSP processors can reduce the data streaming rate to the computers. As imaging is done in real-time, science can be done in real-time with editing and calibrating the

feeds. RFI can be mitigated by implementing digital filters to subtract RFI before averaging and forming nulls in the direction of interferer. Also, a better user interface using real time images can lead to discovery of new sources during observation, and better calibrators and telescopes can be used according to the astronomer's needs and goals.

Chapter 3

The Analog Down-Converters

3.1 Introduction

The recent expansion of the BYU PAF system from 19 elements to 38 elements and space constraints in installing the whole system on radio telescopes led to the idea of developing new receivers, transforming from connectorized components to a printed circuit board (PCB). With the development of new PCB-based receivers, the space requirement for the whole system is significantly reduced compared to the connectorized components base receiver boxes, as the IF filter is now placed on the PCB board itself. The major modification was to use surface-mount components instead of connectorized RF components. Another modification was the use of a single power supply of +5V instead of using 2 different power supplies of +12V and +5V. Since there was no modification in the operating frequencies which made the design process much easier.
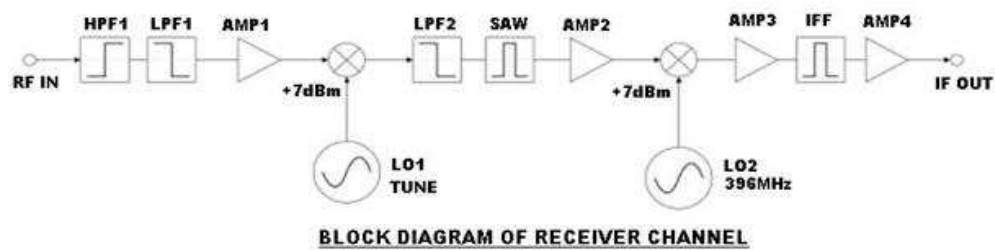
Figure 3.1: The basic block diagram of receiver board.

3.2 Design Overview

The new receiver board is a three stage design, in which first two stages are used for down-converting the signal to a low frequency signal and the third stage is an IF filter, which will be discussed in detail later. The block diagram of the receiver board is shown in the Figure 3.1.

The design is mainly based on the previous receiver design, with some key modifications. The new design includes the IF filter on the board only which eliminates the dc voltage losses from the components, and at least 2-3dB of cable losses. The IF filter band-limits the signal coming in, giving a smooth curve over 425 kHz centered at 2.8125 MHz, the frequency of final IF signal.
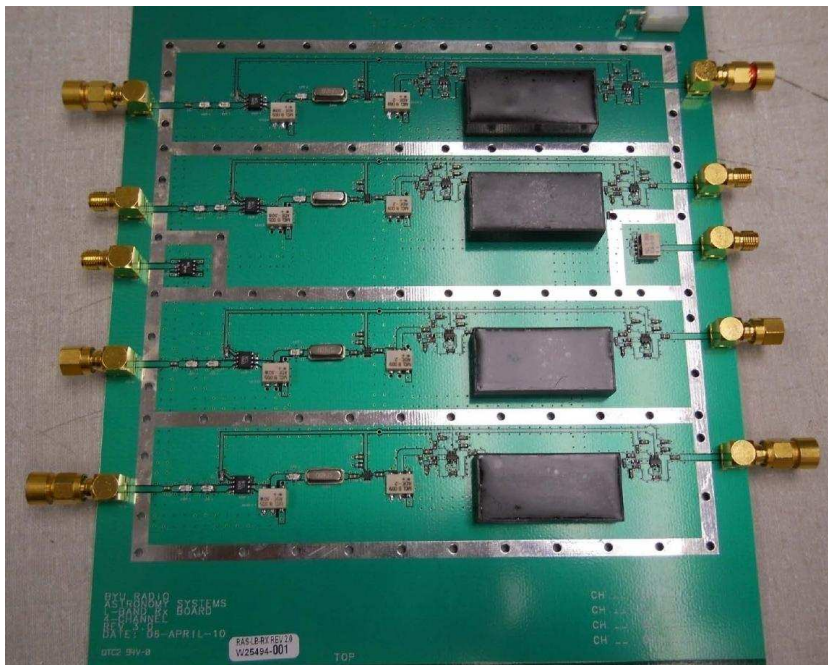
Figure 3.2: The image of the PCB receiver board.

The receiver board is a two layer board, made up of FR4 material of thickness 62 mils, having 1 oz. of copper thickness on each side. The method used in designing the boards is CPWG, which uses the ground layers on both layers, making the transmission losses on board small. The design uses 50 ohm line impedance for the operating range of 0-2 GHz. The dimensions of the board are 233.5 mm x 173 mm (9.192" x 6.8"). Each receiver PCB board consists of 4 parallel RF

Figure 3.3: The schematic of the receiver board.

16

channels, sharing common DC power supply and the IF signals for the mixers. The actual PCB board is as shown in Figure 3.2.

3.3 LO Distribution Network

The LO power distribution to all the four channels on the board is done using four-way power splitters. We use two surface-mount power splitters, one for LO1 and other for LO2, placing them on the opposite side of the board to provide the IF signals to the mixers on each channel. The power splitters are placed in the middle of the boards on each side connected to the third terminal, as can be seen in Figure 3.2.

Mini-circuits BP4P1+ is used for distributing the LO-1 power to the channels. The signal of frequency 2010.8125 MHz at power level of +13.7 dBm is provided to the LO-1 splitter. The LO power required for each channel is only +7 dBm, but this extra +6.7 dBm signal power is to overcome the insertion loss of the splitter at 2000 MHz.

Mini-circuits SCA-4-10+ is used as LO-2 splitter on the board. The signal of frequency 398.8125 MHz at power level of +13.5 dBm is provided to the LO-2 splitter For this second LO, the required power is also only +7 dBm, and this extra +6.5 dBm signal power is to overcome the insertion loss of the splitter at 400 MHz.

The block diagram of the LO distribution network is as shown in Figure 3.3. This figure shows the setup and the parts used for the external LO distribution to split the LO signal coming from the signal generators in ten signal lines to provide the LO signals to ten receiver boards.

3.4 Band Pass Filter

Our range of interest lies in 1400-1700 MHz. Since it is difficult to design a single high-quality band-pass filter over such large range, the first stage implemented in the receiver board is a band-pass filter constructed using a series combination of a high-frequency filter (HPF1) and low-pass filter (LPF1). The high-pass filter used is Mini-circuits HFCN 1200+ and the low-pass filter used is LFCN 1500D+. Both of these are surface-mount components.

The primary purpose of this band-pass filter was to reduce RFI from outside the range of interest, especially around 800 MHz, where RFI is strong. The second purpose was to reject any

17
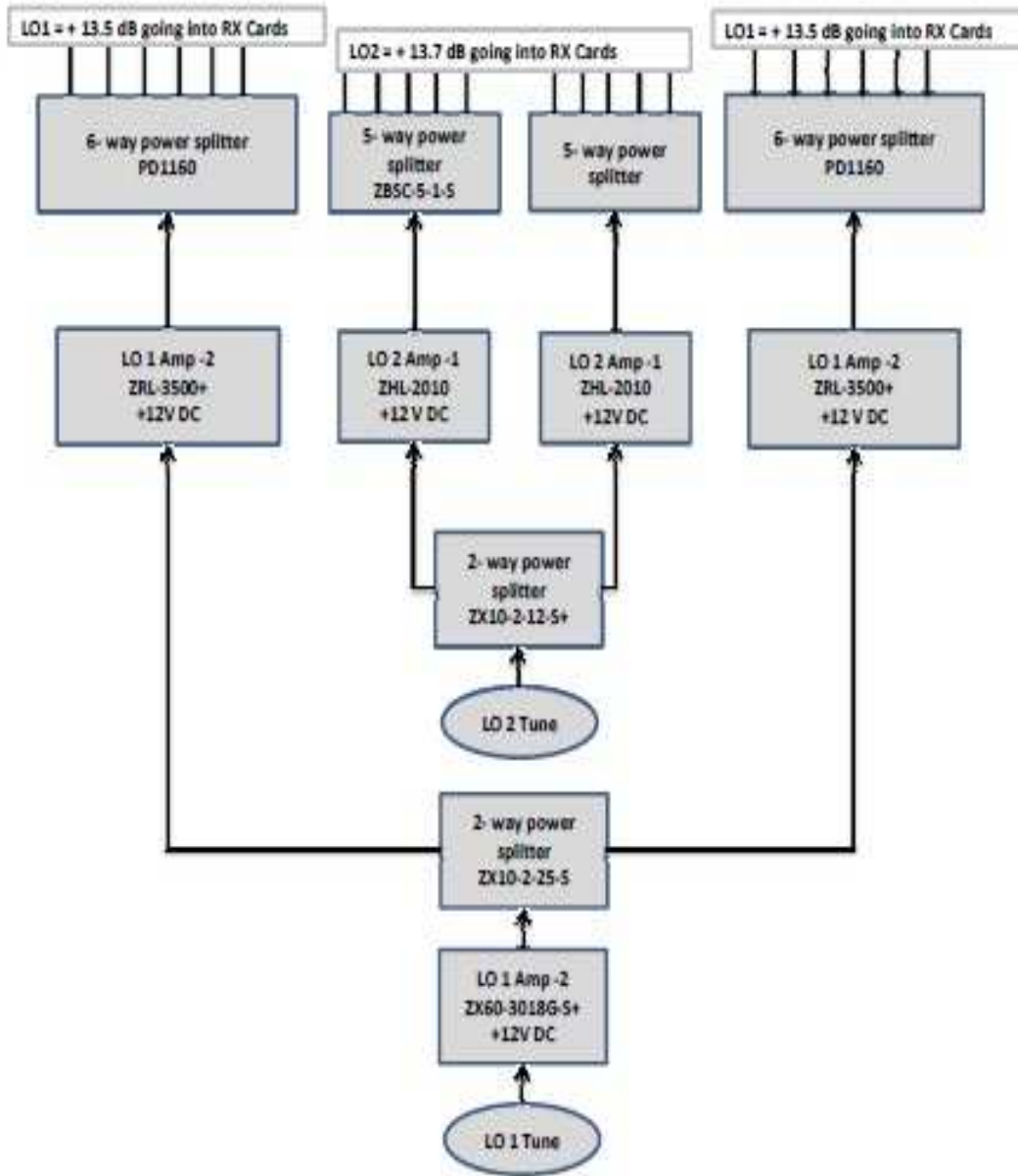
Figure 3.4: The block diagram of LO distribution network.

RFI lying in the image band of the signal. Without this rejection, the image signal would overlap the desired signal after passing from the first mixer [17].
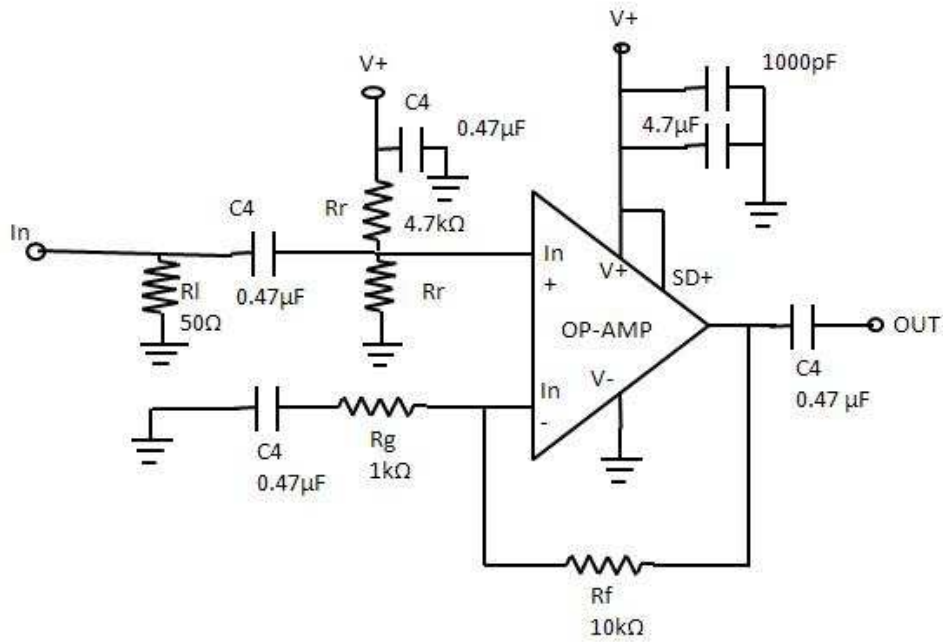
Figure 3.5: The amplifier design using an op-amp circuit, used on the receiver boards for providing final gain stages.
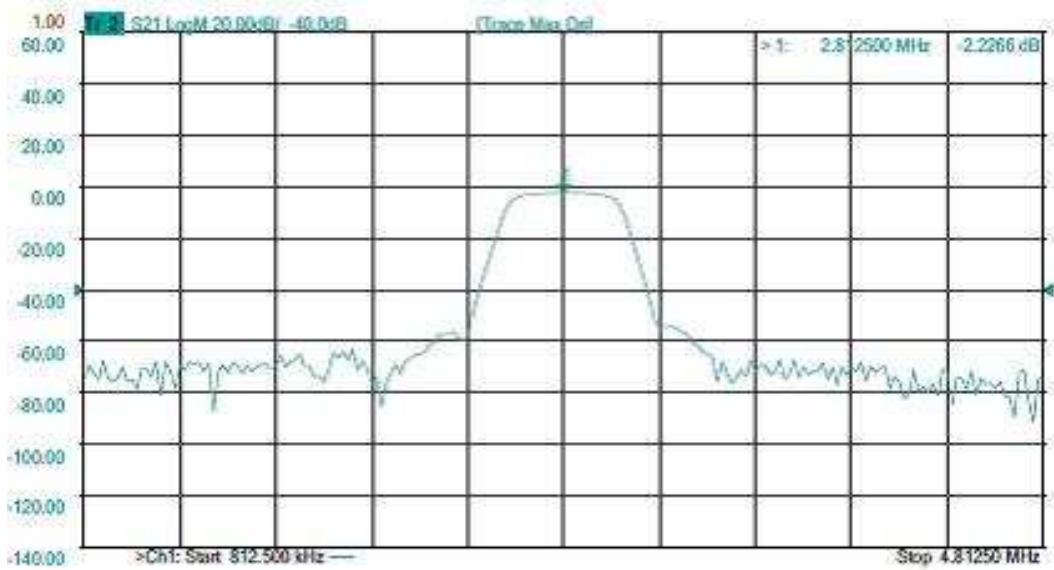
Figure 3.6: The frequency response curve of the IF filter.

3.5   First-Stage Down Conversion

The first down conversion stage is the combination of the amplifier AMP1 and mixer MIXER1. The first amplifier used is Mini-circuits VNA-28, giving a gain of +22.8 dB at a frequency of 1.5 GHz and has the noise figure of 3.7 dB. A capacitor of 0.01uF was used on the DC supply to bypass DC current.

Mixer 1 is Mini-circuits ADE 30W+, having the specified LO power supplied at +7 dBm and has a conversion loss of 6.7 dB. For the RF signal at 1612 MHz, the IF signal coming out of the mixer is at 398 MHz when the LO signal is supplied at 2010 MHz.

3.6   Second-Stage Down Conversion

The second stage down converter consists of low-pass filter LPF2, a surface-wave-acoustic filter (SAW), another amplifier AMP2 and mixer MIXER2. The low pass filter used is Mini-Circuits LFCN-530+, which has the insertion loss of 0.60 dB. The SAW filter used is Vanlong SF-400, which is a very high-Q bandpass filter. It is a through-hole component, for which the ground connections are made on the bottom ground plane.

The bleed-through signal from the LO input on mixer 1, a very strong signal at the output of the SAW filter, made it necessary to have a separate low-pass filter to reject the high-frequency signal from going into the SAW filter [17]. The SAW filter has an insertion loss of 3.5dB.

The second amplifier AMP2 used is Analog Devices Inc.'s AD8354ACPZREEL7CT-ND. The amplifier provides the gain of 20 dB. The AC coupling capacitors are put on both the input and output signal lines to isolate the DC bias. The voltage supply is decoupled using a parallel combination of DC bypass capacitors.

The final device in this stage is Mixer 2. The device used is Mini-Circuits ADE-2+, having a conversion loss of 6.7 dB. The LO power is supplied at +7dBm.

3.7   Third-Stage IF Filter

The third stage consists of an amplifier AMP3, an IF filter and another amplifier AMP4. The amplifiers AMP3 and AMP4 are implemented using an operational-amplifier feedback designed to provide a gain of 20dB. The op-amp circuit is shown in Figure 3.5. The op-amp used

is National Semiconductors LMH6639MFCT-ND. The op-amp is implemented in a negative feed-back configuration. The voltage supply is decoupled using a same configuration as used in AMP2.

The final IF filter in the system is a Band-pass filter from KR Electronics. The overall response of the filter is as shown in the Figure 3.6. The center frequency of the filter is 2.8125 MHz, with 3-dB bandwidth of 425 kHz $\pm$ 10% . The insertion loss is less than 3.5 dB. Since this component is now placed on the board itself, it has reduced the space requirements to a large extent. The cable requirements and the losses associated with them have become significantly reduced. The filter comes in an epoxy case and is a through hole mounting component using the bottom copper layer on board as the ground plane.

3.8   PCB layout

The layout of the receiver board is as shown in Figure 3.7. ADS 2009 (Agilent, Inc.) was used to design the layouts of the board. Gerber files were generated and exported, and were used by the fabrication and assembly units for manufacturing the boards.

3.9   Parts List

Table 3.1 shows the list of all the parts used on the receiver board. It shows the part numbers of all the components used on the board, their vendors, number of units used on each board, the price per unit, total cost and type of mounting used by the component. The total cost for one receiver board with four channels is $516, much less in comparison to old receiver boxes for two channels which cost around $2000.

3.10   Tests

As the receiver boards have four channels on each, it was important for the boards to have low cross-coupling in between the channels. To check this, the boards were connected to DC supply, and the signal input of -65 dBm is given at one of the RF inputs with all other terminals terminated with a 50 ohm SMA terminator. The output is checked using spectrum analyzer, at each of the four outputs to find out the cross coupling between channels. The average cross-coupling between the channels is found to be lesser than -40 dB.

Table 3.1: Parts list of the receiver board.

Item	Part Name	Part Number	Vendor	# of Units	Price/Unit	Price/ PCB Board	Type
1	PCB Board	FR4	Quick Turn Ckts.	1	45	45	
2	PCB Board Assembly		Precision Assembly	1	43	43	
3	HPF 1	HFCN 1200+	Mini Circuits	4	1.99	7.96	Surface Mount
4	LPF 1	LFCN 1500D+	Mini Circuits	4	3.19	12.76	Surface Mount
5	AMP 1	VNA-28	Mini Circuits	4	1.90	7.60	Surface Mount
6	MIXER 1	ADE-30W+	Mini Circuits	4	8.45	33.80	Surface Mount
7	LPF 2	LFCN 530+	Mini Circuits	4	2.69	10.76	Surface Mount
8	SAW	SF 400	Van Long	4	4.22	16.88	Through Hole
9	AMP 2	AD8354ACPZ-REEL7CT-ND	Digikey	4	1.23	4.90	Surface Mount
10	MIXER 2	ADE 2+	Mini Circuits	4	2.29	9.16	Surface Mount
11	Connectors	ACX1232-ND	Mouser	10	3.84	38.40	Through Hole
12	AMP 3 and Amp 4	LMH6639MFCT-ND	Digikey	8	1.23	9.84	Surface Mount
13	R1	71-CRCW0603-50-E3	Mouser	8	0.03	0.24	Surface Mount
14	C1	490-1495-1-ND	Digikey	12	0.03	0.41	Surface Mount
15	Rg	P1.0KDBCT-ND	Digikey	8	0.12	0.95	Surface Mount
16	C2	709-1152-1-ND	Digikey	8	0.025	0.20	Surface Mount
17	Rf	P10KDBCT-ND	Digikey	8	0.12	0.95	Surface Mount
18	C3	399-5503-1-ND	Digikey	12	0.17	2.03	Surface Mount
19	DC In	538-39-30-1020	Mouser	1	0.65	0.65	Through Hole
20	DC In Adapter	538-39-01-2020	Mouser	1	0.24	0.24	Adapter
21	C4	490-1540-1-ND	Digikey	40	0.05	2.01	Surface Mount
22	LO Split 1	BP4P1+	Mini Circuits	1	1.44	1.44	Surface Mount
23	LO Split 2	SCA-4-10+	Mini Circuits	1	6.45	6.45	Surface Mount
24	IF Filter		K.R.Electronics	4	65	260	Through Hole
24	Rr	P4.70KHCT-ND	Digikey	8	0.02	0.18	Surface Mount
	Total					516	

Table 3.2: Gain of the channels on one receiver board.

	Input	Output	Gain
Channel 1	-65 dBm	-3.1 dBm	61.9 dB
Channel 2	-65 dBm	-2.62 dBm	62.38 dB
Channel 3	-65 dBm	-2.78 dBm	62.22 dB
Channel 4	-65 dBm	-1.90 dBm	63.1 dB

Table 3.3: Cross coupling between the channels on one receiver board.

	1	2	3	4
1	-2.82	-50.9	-56.8	48.8
2	-50.6	-2.36	-45.6	-51.9
3	-55.3	-45.2	-2.99	-49.3
4	-45.8	-52.2	-57.2	-1.6
*Input = -65 dBm				

Table 3.4: Gain and noise figure of the channels on one receiver board.

	Gain	Noise Figure
Channel 1	53.2 dB	11.6 dB
Channel 2	53.9 dB	11.9 dB
Channel 3	52.3 dB	12.7 dB
Channel 4	54.2 dB	11.5 dB

Table 3.5: Comparison of T_{rec} temperature between old and new receivers.

	Old RX Box	Old RX Box with DAQ	New RX cards	New Rx Cards with DAQ
T_{rec}	1809 K	4545 K	1724 K	2998 K
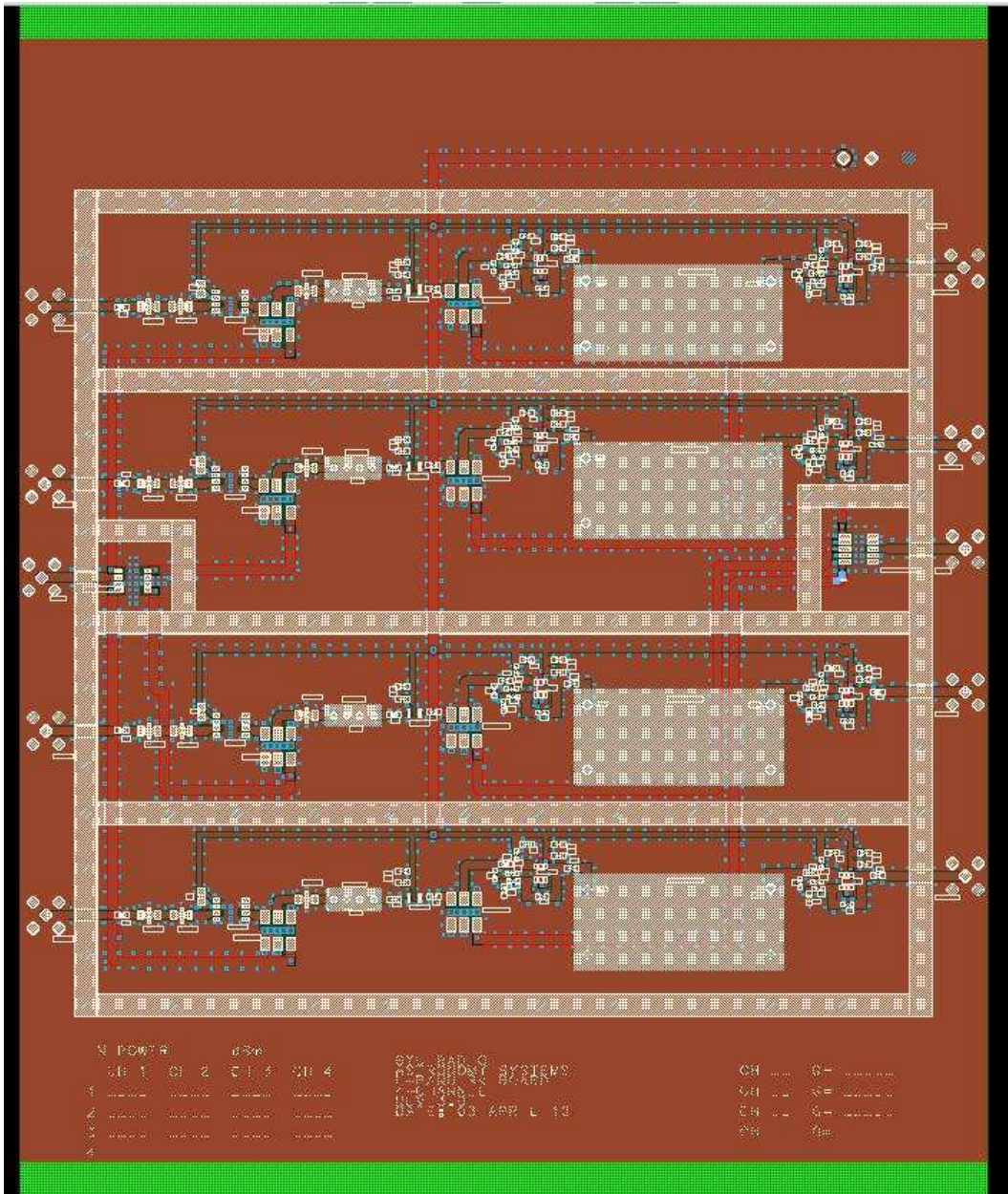
Figure 3.7: A snapshot of the layout of the receiver board from ADS.
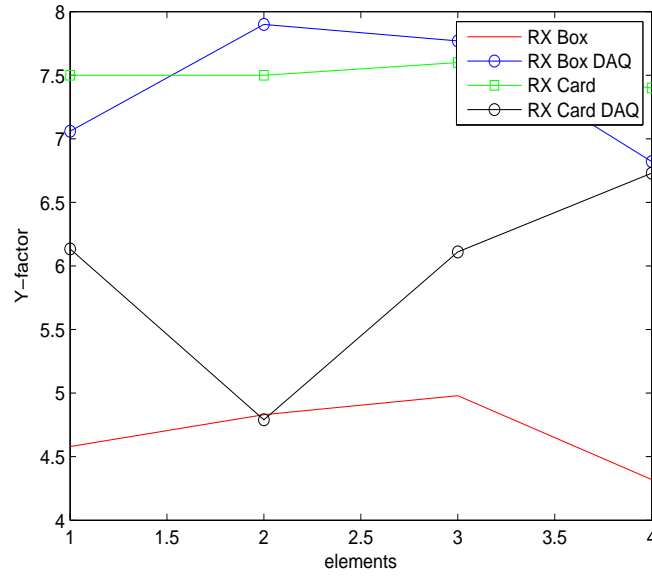
Figure 3.8: Figure shows the comparison of Y-factor values between the old and new receivers.

The noise figure of the receiver boards was measured using a noise figure measurement instrument at Arecibo Observatory, Arecibo, Puerto Rico. The method used was same as the above, except for using the noise figure measurement instrument instead of spectrum analyzer.

The tables 3.2 to 3.4 show the results obtained for average gain of the channel, cross coupling between different channels on the board and the noise figure of the channels. Table 3.2 shows the gain of each channel on a single receiver board. Table 3.3 shows cross coupling between the channels on the board. It shows the output values at each channel when one of the input is given the signal with rest of the terminals terminated. Table 3.4 shows the gains and noise figure of each channel on a single board measured using the noise figure measurement instrument.

Figure 3.8 shows the comparison of the Y-factor measurements between the old receiver boxes and new receiver boards. The measurements were taken using the old data acquisition system. The input signal was given using HP noise source. It can be seen from the figure that receiver card have lower Y-factor in comparison to the receiver boxes. Figure 3.9 shows the comparison of the T_{rec} values between the old and new receivers. The value of T_{rec} was calculated using the Y-factor values. The receiver cards were found to have lower temperatures in comparison to the
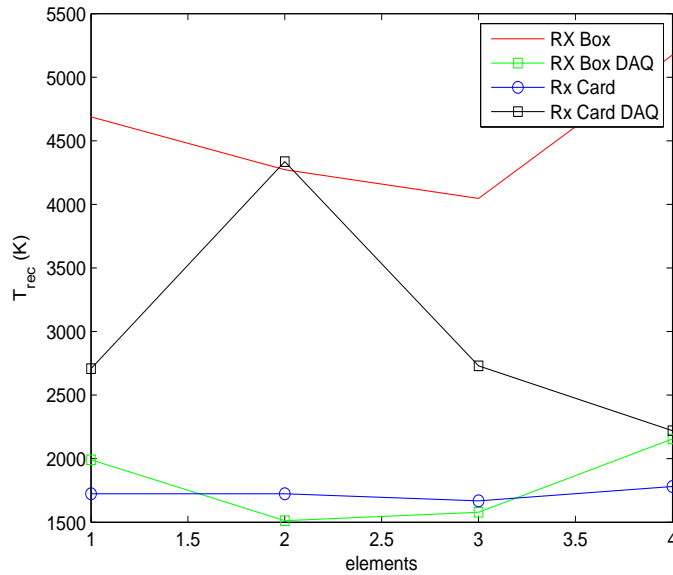
Figure 3.9: Figure shows the comparison of T_{rec} values between the old and new receivers.

receiver boxes. Table 3.5 shows the comparison of T_{rec} values between the old receiver boxes and new receiver boards.

3.11 Conclusion

A total of twelve receiver boards were manufactured and were used for the experiments done at Arecibo Observatory in June-August, 2010 and at Green Bank in January and April-May, 2011. They were used as down-converters for all the phased array feeds. The performance of the receiver cards was stable and provide a good performance for long as well as short observations.

Since a new digital backend is in development, which will be a CASPER FPGA-based ROACH board system for real-time data processing and the band of interest will be increased to 20 MHz, these boards will not be able to work with that system mainly because of the SAW filter and the IF filter used on the boards which limit the performance bandwidth. Thus, a new receiver board is being developed with these key modifications to make it work with the new digital back-end.

Chapter 4

The Feasibility Study of Phased Array Feed

4.1 Introduction

As the PAF systems are developed for radio astronomers, it is necessary to check out the proper functioning and performance of the whole system by doing on-site experiments. The on-site experiments refer to mounting and installing the whole system - antennas, backend down-converters and data acquisition system - at the site, collecting data using the system and doing post-processing of the data to produce new results. These results help to continue the development of new feeds and signal processing techniques for the use of PAFs for the radio astronomy. The 20-meter telescope and 100m telescope at Green Bank, West Virginia and 300m telescope at Arecibo Observatory, Arecibo, Puerto Rico are the major sites which are extensively used by the radio astronomers for the observations. Thus, it is necessary for us to use these sites for our experiments and analysis.

The experiments at 20m telescope at Green Bank, WV and the experiments at Arecibo Observatory, Arecibo were part of one such effort to find out the compatibility and other important characteristics needed to develop a new PAF for both the observatories. The experiments at Arecibo, PR were conducted in the month of June, 2010 and in latter part of August, 2010 and the experiments at Green Bank, WV took place in January, 2011 and April, 2011.

4.2 Weak Source Imaging

The capability to image weak sources using the PAFs is one of the major problems faced by the radio astronomy community to use PAFs on radio telescopes. This section discusses a way that can be used to form images of weak sources. To accomplish this, two sources are required to form an image of the weak source. The beamformer weights are found using a calibrator source

and then these weights are applied to the weak source correlation matrix to calculate out the power at each pointing in the grid. This power obtained is used to form the image of the weak source.

In practice, the weak sources are observed generally by doing a slice cut on the source in either zenith or azimuth with off-pointings at the start and end of the slice. The signal correlation matrix $\mathbf{R}_\text{v}^\text{s}$ is obtained by subtracting the off pointing correlation matrix $\mathbf{R}_\text{off}^\text{s}$ from the on-pointing correlation matrices $\mathbf{R}_\text{on}^\text{s}$, so that

$$\mathbf{R}_\text{v,n}^\text{s} = \mathbf{R}_\text{on,n}^\text{s} - \mathbf{R}_\text{off,n}^\text{s} \tag{4.1}$$

where superscript s stands for weak source data and n stands for the pointing index.

The power in the weak source data at each slice point, is projected on the calibration grid and the images are formed. The power calculated for the weak source at each calibration grid point, can be given by

$$P_\text{n}^\text{s} = \mathbf{w}_\text{n}^H \mathbf{R}_\text{v,n}^s \mathbf{w}_\text{n}. \tag{4.2}$$

One problem associated with this process of imaging weak sources is the difference in the noise levels in the data obtained from the two sources. Since the noise level around the sources is not stable and differ at every point in the sky, the noise levels differ in two observation sets. To analyze the change in the noise over time, the same power calculation process is repeated for the correlated data with a number of short time integrations (STIs), and the corresponding power values are stored in a different matrix. This calculation provides us with the data to study the variability in the system over time. As a check, we need to make sure that the noise level in both the data sets is almost same. This is done by comparing the system equivalent flux density (SEFD) values:

$$\text{SEFD}^\text{s} = \log_{10}(c_n \mathbf{w}_\text{n}^H \mathbf{R}_\text{off}^\text{s} \mathbf{w}_\text{n}) = 2.6403 Jy \tag{4.3}$$

$$\text{SEFD}^\text{c} = \log_{10}(c_n \mathbf{w}_\text{n}^H \mathbf{R}_\text{off}^\text{c} \mathbf{w}_\text{n}) = 2.6523 Jy \tag{4.4}$$

where c_n is the constant obtained from

$$F^\text{c} = c_n P_\text{n}^\text{c} \tag{4.5}$$

where F^c is the flux density of calibration source, generally CasA having flux density of 1460 Jy. This constant c_n is used to convert the power obtained from weak source into the units of flux

density(Jy), denoted by F^{s}, using

$$F^{s} = c_{n}P^{s}_{n}. \tag{4.6}$$

Since the constant c_{n} has different value for every beamformer, the flux density is calculated at each grid point.

4.3 Noise Variability

The noise floor should be stable over the observation period ideally, but in practice, it is variable over the sky area and varies with time. This section discusses the calculations done on the correlated data set of image source to study the variation of the noise floor over the grid. For this, the grid points in which there is a source are excluded. This provides us with the noise-only data with the concentration only in the field of view (FOV).

Since the grid is much larger than the actual FOV of the dish, the grid is reduced by retaining only the pointings which constitute the FOV of the dish. In the case presented here, the FOV is 0.9 degrees on each side to the center of the grid, which make it a 7x7 grid around the center position. The values corresponding to this 7x7 grid are stored in different matrix F^{FOV} and standard deviation of these values is taken over the whole slice, which provides us with the variation in power ΔP^{s}. The standard deviation of the power can be calculated as

$$\Delta P^{s} = \mathrm{std}_{\mathrm{n \in FOV}}(\mathrm{P_{n}}) \tag{4.7}$$

and the mean of this standard deviation of power is taken over increasing number of STIs. This is compared to the theoretical curve which is given by

$$\Delta P = \alpha \frac{F^{\mathrm{weak}}(\mathrm{Jy})}{\sqrt{N}} \tag{4.8}$$

$$= \alpha \frac{F^{\mathrm{weak}}(\mathrm{Jy})}{\sqrt{Bt_{\mathrm{int}}}} \tag{4.9}$$

where F^{weak} is the flux density of the weak source, B is the system bandwidth and t_{int} is the integration time, which is a function of number of short time integrations (STIs) integrated, and α is a constant and is approximated to be equal to unity depending on certain parameters.

Figure 4.1: The aerial view of Arecibo Observatory.

4.4 Experiments at Arecibo Observatory

4.4.1 Arecibo Observatory

Arecibo Observatory is a part of the National Astronomy and Ionosphere Center (NAIC), a national research center operated by Cornell University under an agreement with National Science Foundation (NSF). The observatory operates on a 24x7 basis for the whole year except maintenance time, providing observing time, electronics and computer to scientists from all over the world. The observatory is recognized as one of the most important national research center for radio astronomy and as the site of world's largest single-dish radio telescope.

The main spherical reflector is 305m in diameter, 167 feet deep, made up of almost 40,000 perforated aluminum panels supported by a network of cables under the dish. The dome and the antenna platform are suspended 450 feet above the reflector. The dome hangs mid-air on eighteen cables, strung from three concrete towers. The azimuth arm is a bow shaped 328 feet long structure,
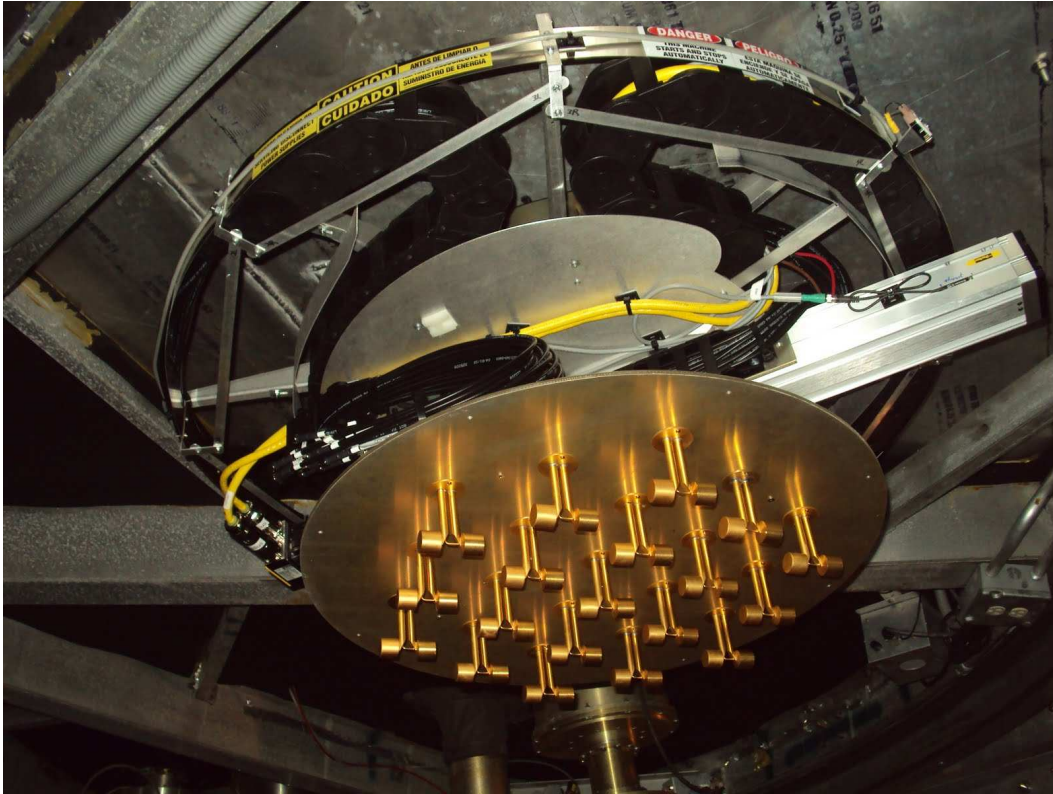
Figure 4.2: The positioner installed on the platform to move the PAF to different positions.

attached below the triangular frame. The curved path provides another path on which the dome can be moved upto 20 degrees from the vertical.

The dome carries all the horn feed antennas and other antennas, which are connected to radio receivers. Also, the secondary and tertiary reflectors, inside the dome, are used to focus to point in the sky. The large size of the reflector make the Arecibo telescope most sensitive radio telescope in the world, as enough energy can be collected by the telescope within few minutes in comparison to hours of observation time required by other telescopes.

4.4.2   Experimental Setup

Since Arecibo telescope is 305m in diameter, the 19-element BYU-PAF array was not sufficient to cover the whole reflector and to provide the required measurements due to its small size. So Dr. German Cortes, at Cornell University, came up with the idea to use a bigger hexagonal pattern, which was made by arranging the 19-element hexagonal array to form a bigger hexagonal
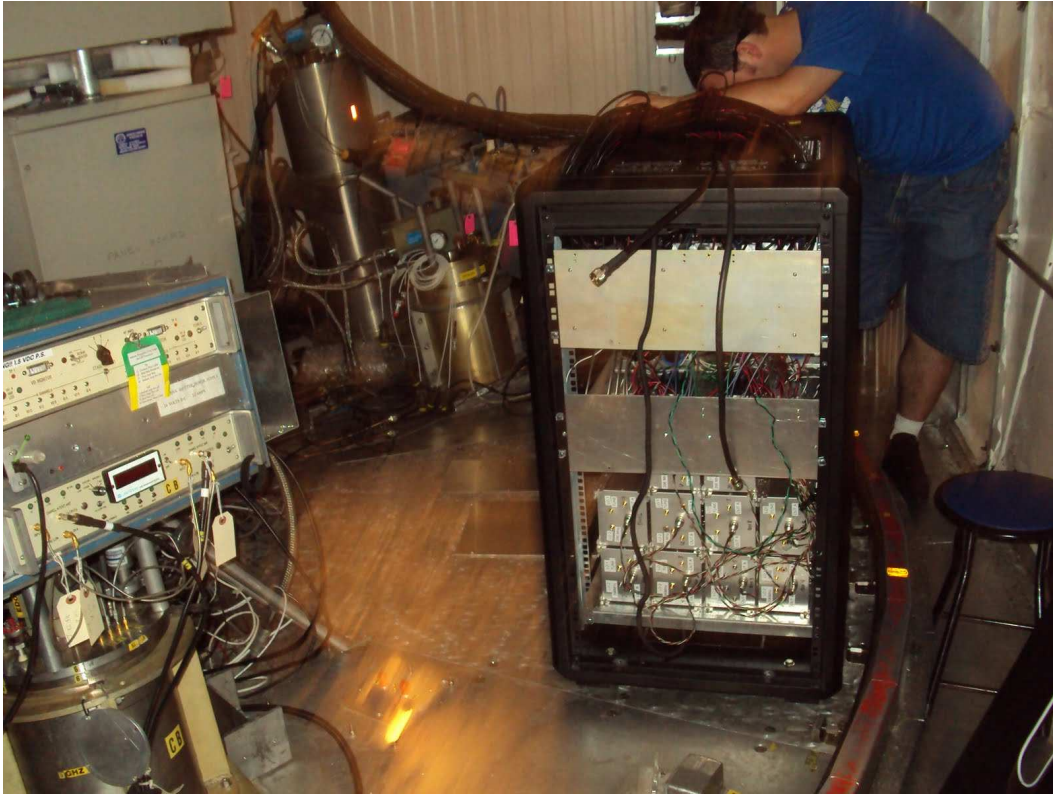
Figure 4.3: The receiver rack installed on the lower floor of the dome. It has the new receiver cards rack, LO distribution for the receiver cards, old receiver boxes, power supply for the LNAs.

array which could be used as an image of the actual feed, as shown in figure 4.2. To take the data from all the positions, it was not physically possible to move the array to the position every time, so a movable platform was developed. This platform was designed to move the array from one position to another in horizontal plane and also in the vertical plane. The platform is as shown in the figure 4.3.

The other major setup involved the setup of analog receivers and the data acquisition setup. The analog receivers were put in a small rack, along with the LO distribution network and the power supply for the low noise amplifiers (LNAs). This rack was setup just beside the moving platform on the lower floor of the dome. The data acquisition rack, containing all the acquisition computers and a hub, was installed on the upper floor of the dome. It was connected to the local intranet network by a fiber optic system. These computers were directly controlled remotely from the control room during observation hours.
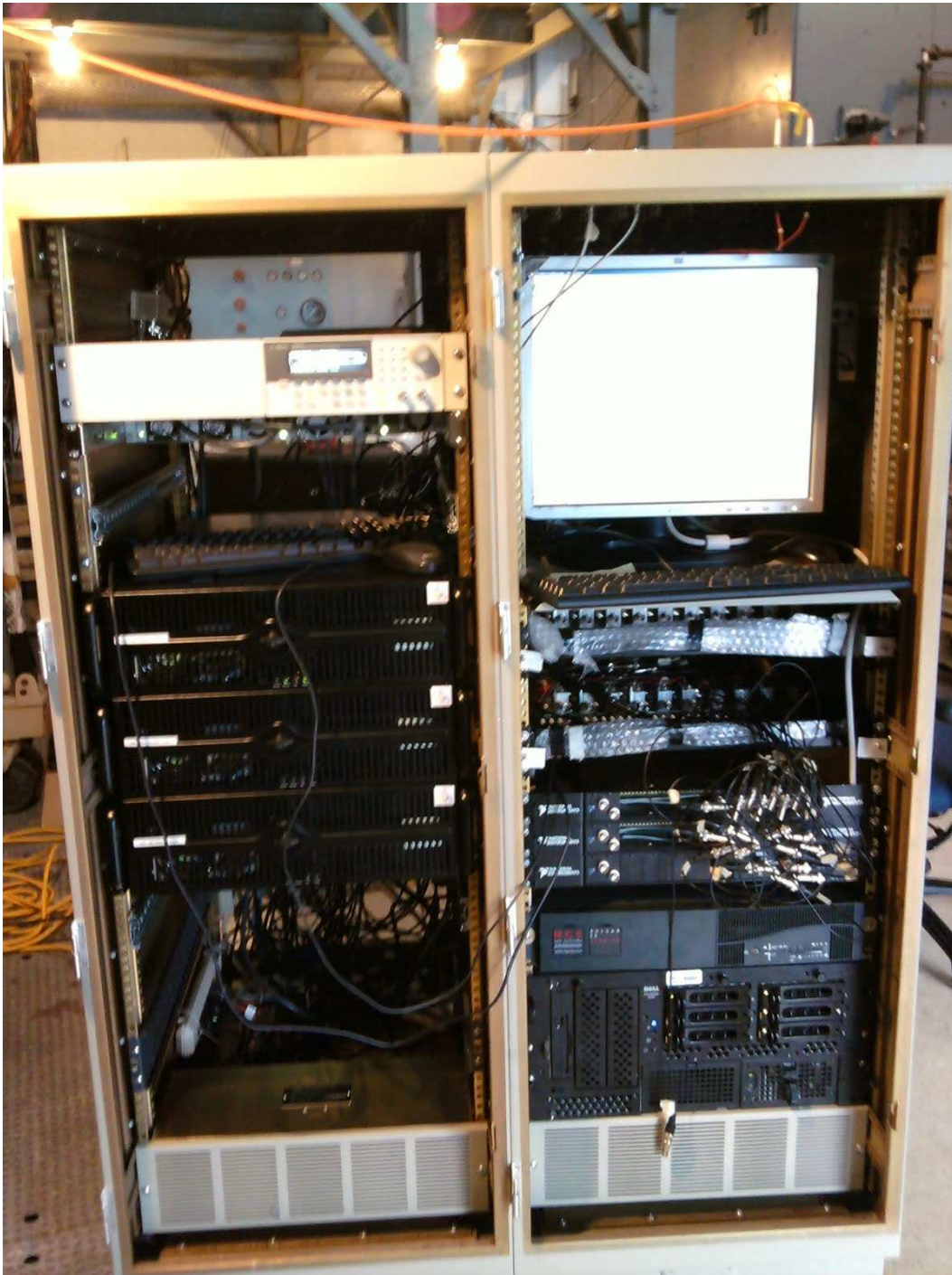
Figure 4.4: The data acquisition rack with acquisition computers and a hub, along with the old data acquisition computer and IF trays. It also has the function generators and a monitor installed, in case to debug the system. This rack was placed on the upper floor of the dome.
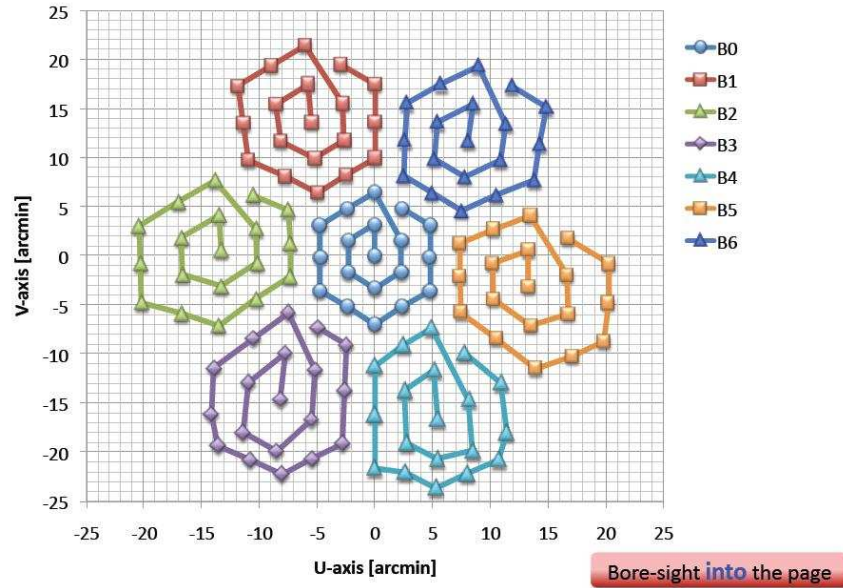
Figure 4.5: The image of the weak source formed using a 1x51 slice on a weak source grid [1].

All the antenna channels were connected to the receiver cards as inputs. The down converted IF output from the receiver cards was connected to the ADC cards on the computers on the upper floor. The cables were run through a cable wrap to keep them away from tensions in the cables, as the dome moves.

4.4.3   Observations and Data Taking

The actual observations and data taking took place in two phases. The first phase lasted from June 14, 2010 to June 26, 2010 after all the setups were completed and verified, and the second phase took place from August 19, 2010 to August 26, 2010. A lot of time was required to synchronize the communications between the data acquisition and the telescope control computer. Enough time was also spend on getting the movable platform set-up and in setting up its communication with the telescope control computer and to verify movement of array to different array positions.

The observations were first started with single-pole array and the unprocessed data was collected on the computer. The observations usually started in the evening and continued till early morning hours. The data collected was then transferred to the portable hard drives and then correlated. The list of the different observations is as follows:

34

- A coarse grid of 7x7 pointings on a source with off pointings at the start and the end of the grid, done at all the array positions.

- A fine grid of 15x15 pointings on a source with off pointings at the start and the end of the grid, done at all the array positions as shown in Fig. 4.5.

- A superfine grid of 31x31 pointings on a source with off pointings at the start and the end of the grid, done at the array's A0-A6 positions.

- A slice of 15x1 pointings on weak source with off pointings at start and the end

- Observation of extended sources for forming mosaic images.

- Frequency scan over a range of 700 MHz on to a same source with off pointings at start and end.

- Hot-Cold noise measurements of array using an absorber as a hot environment.

- Observations in Z-plane to locate the ideal focus point.

(a) Single pol array mounting reference

(b) Dual pol array mounting reference
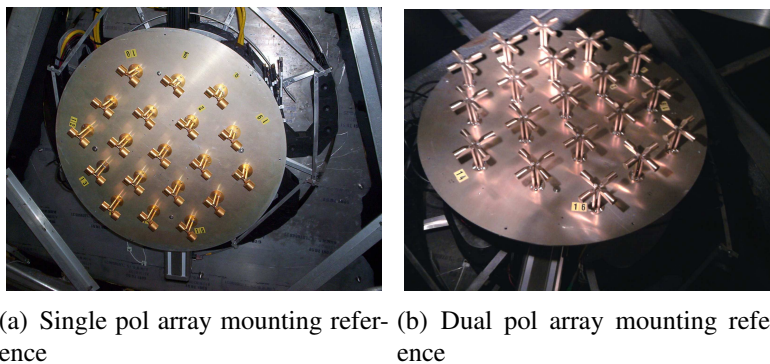
Figure 4.6: Figure shows the images of (a) single polarized array, and (b) dual polarized array mounted on the positioner at the primary reflector of the Arecibo dish.

This data was taken using old data acquisition system which uses NI ADC cards and LAB-VIEW software. As a step to check and verify the new data acquisition, some of these grids were repeated with the new system.

The single polarization array was replaced with the dual polarization array for the last two days of data observation during first phase and the data was taken using different configurations of dual polarization array - A configuration (all A-polarization of dual pol array), B configuration (all A-polarization of dual pol array) and AB configuration (all A- and B-polarization of inner 7 elements of dual-pol array).

The second phase of data acquisition in August, 2010 took place in the same manner with both single and dual pole arrays. The main focus was put on taking superfine grids for all of the A-positions with the single pole array and taking data for all the coarse grids at A- and C- positions with the dual pole array.

4.4.4 Experimental Results

All the data taken was correlated and analyzed in post-processing. Figure 4.7 shows the sensitivity of the single-pol array at different positions from A0-A6. The sensitivity was calculated from the superfine grid data having 31x31 pointings on the source. All the plots showed a small dough-nut shape hole in the plots, for which the exact reason was not clear, whether it was due to the low-sensitivity associated with the dipole at that position or due to the fault in receiver electronics.

Figure 4.8 shows the images of the calibration and the weak source. The image of the calibration source was formed using the calibration source data. The beamformer coefficients were calculated using the same calibration source data. The image of the calibration source was formed at the boresight position. The weak source image was formed using the weak source data and the same beamformer coefficients from the calibration source as discussed in Sec 4.2. The weak source can be seen in the image but has a very low intensity.

Figure 4.9 shows the standard deviation of the averaged noise floor over the increasing number of STIs. The analysis was done as discussed in Section 4.3. The noise floor showed the constant fall in the value as the number of STIs increase but it was much higher as compared to the analytical value, which can be seen in the Figure 4.10.

The feasibility study also included designing a road map for the digital backend requirements, its architecture and the functions it may do with the A040 phased array feed. This digital backend is discussed in detail in the next chapter.

36

(a) A0 position

(b) A1 position

(c) A2 position

(d) A3 position

(e) A4 position

(f) A5 position
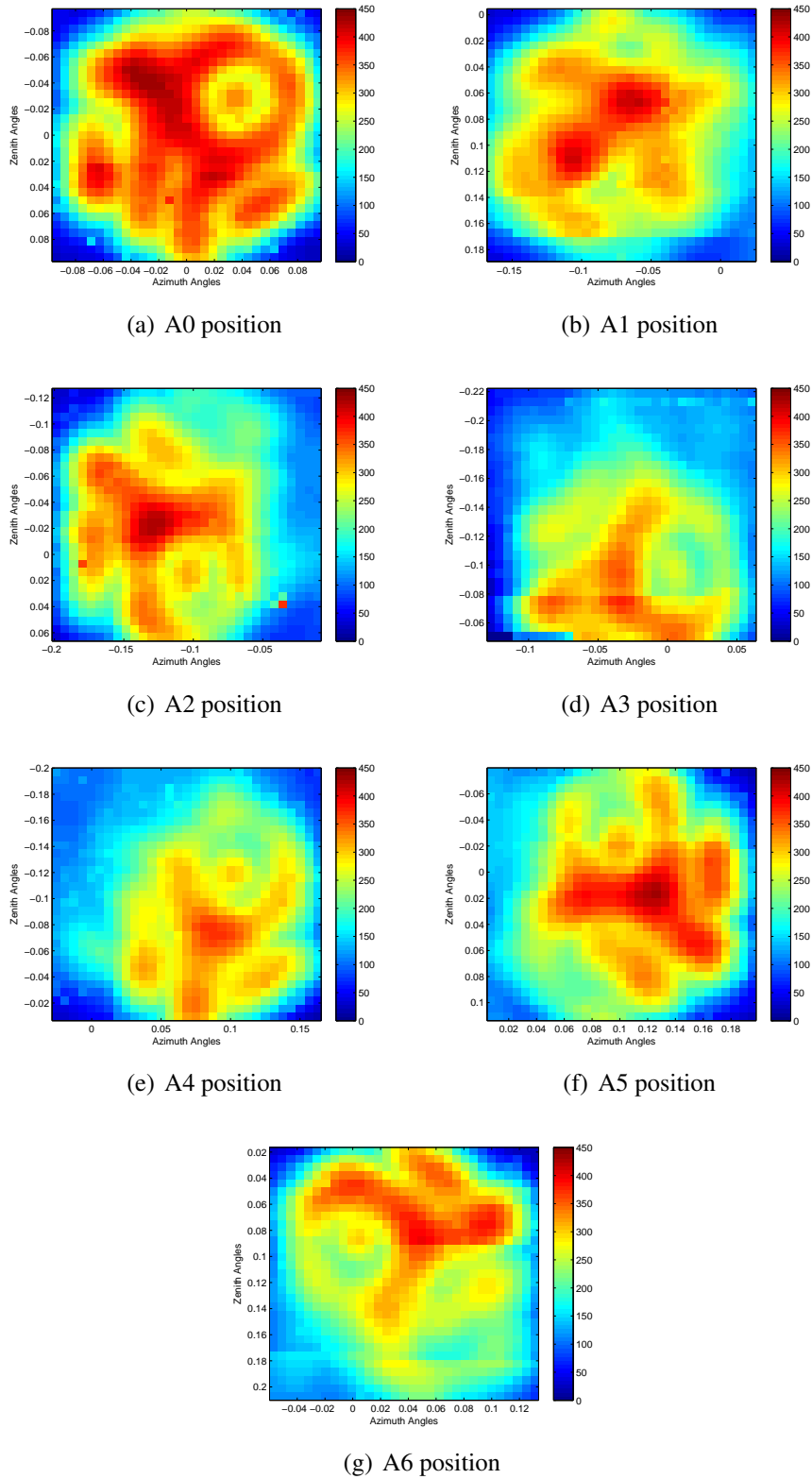
(g) A6 position

Figure 4.7: Figure shows the sensitivity of the single-pol array at Arecibo in A0-A6 positions for 31x31 superfine grid observations.
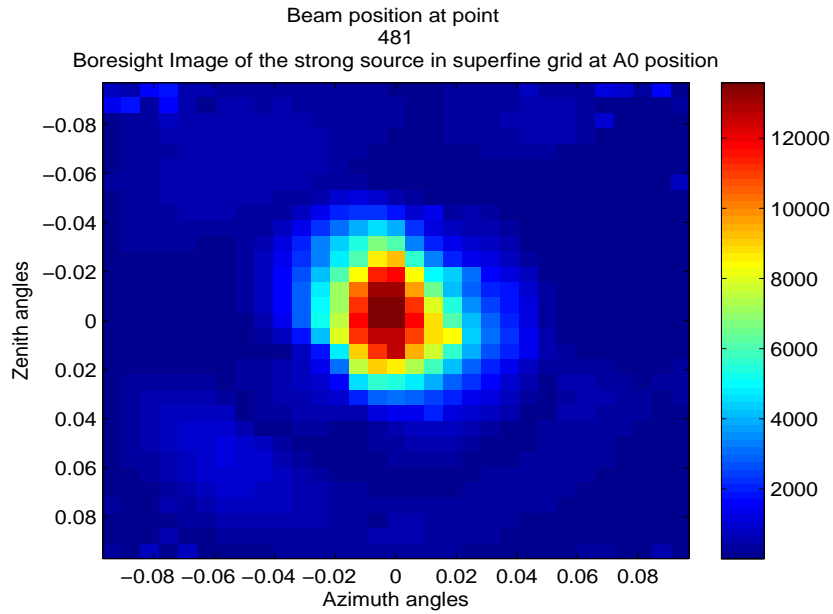
(a) Boresight image of the calibration source
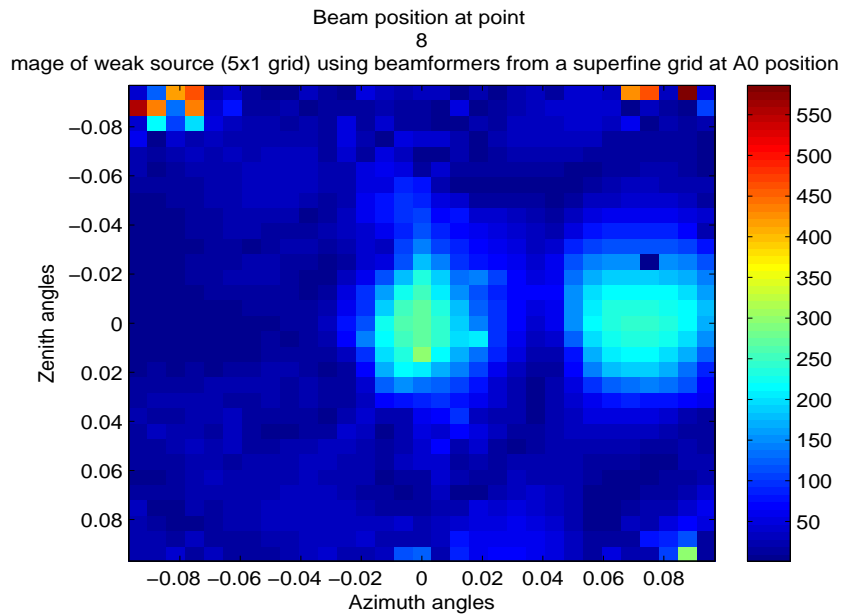
(b) Image of the weak source

Figure 4.8: Figure (a) shows the boresight image of the calibration source formed using calibration data, and (b) shows the image of weak source formed using the weak source of 10 Jy and the beamformer weights calculated from the calibration source data.
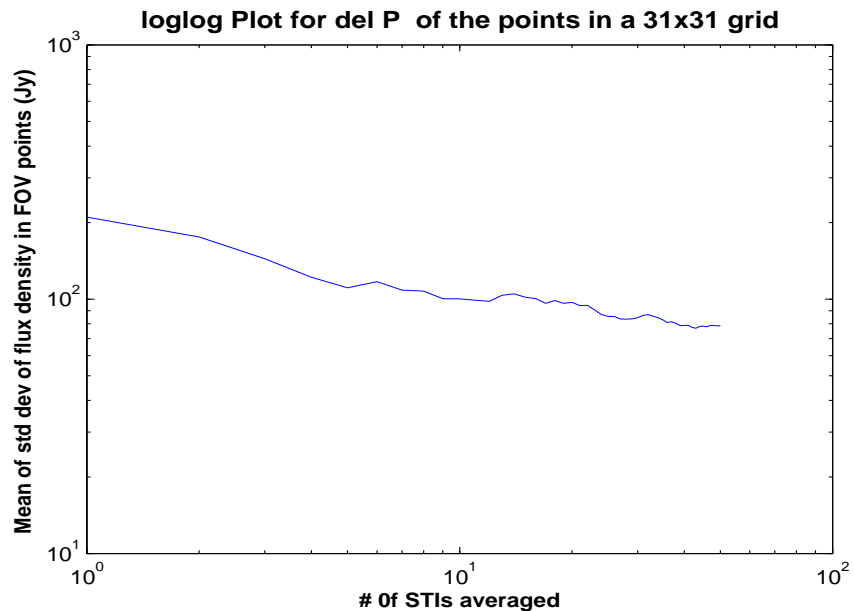
Figure 4.9: Figure shows the logarithmic plot of the standard deviation of the noise over increasing number of STIs.
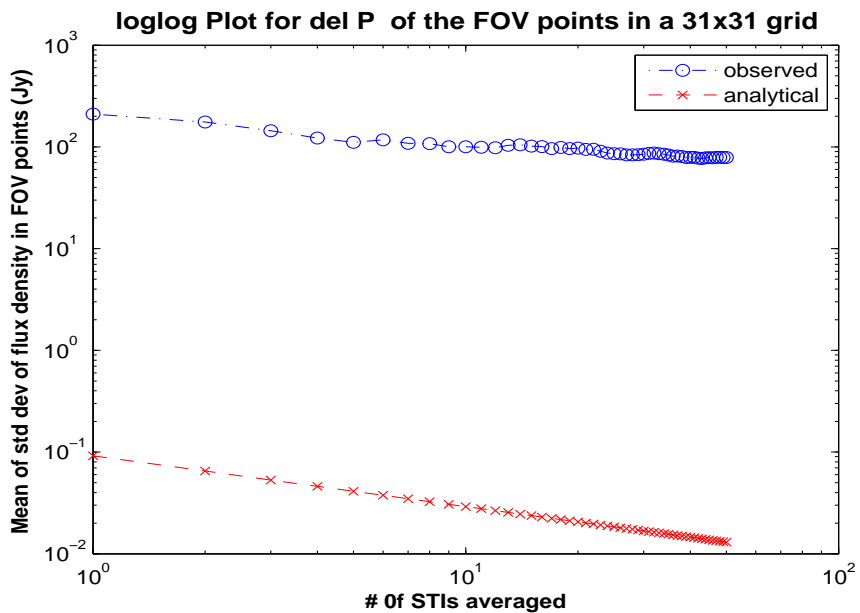
Figure 4.10: Figure shows the comparison between the logarithmic plot of the standard deviation of the noise over increasing number of STIs and the analytical noise field.

4.5 Experiments at Green Bank 20-m Dish

4.5.1 20-meter Dish at Green Bank Observatory

The Green Bank Observatory is a part of the National Radio Astronomy Observatory (NRAO), operated under agreement with the Associated Universities, Inc. for radio astronomy. The observatory leads the research in the scientific study of pulsars, dense neutron stars. The observatory contains many notable telescopes, among them are the Robert C. Byrd Green Bank Telescope (GBT), the world's largest most technically advanced fully-steerable single-dish radio telescope, 140-foot (43 m) equatorial mount radio telescope, the Green Bank Interferometer formed using three 85-foot (26 m) telescopes, a 40-foot (12 m) telescope for educational purposes and a 20-meter radio telescope.

The GBT is 110-meter by 100-meter dish weighing 17 million pounds, collecting weak astronomical radio waves from the Universe. The wheel and track design of the GBT allows it to view the entire sky above 5 degrees elevation. The dish has an off axis feed projecting from one edge which increases the total useful area of the telescope. It has a highly sensitive receiving system protected from radio frequency interference, as it is located in the national radio quiet zone. The GBT is able to detect the fingerprints of atoms and molecules far into the distant Universe, yielding new knowledge about star formation, the structure and motions of gas in galaxies, and Nature's fundamental constants.

The 20-meter radio telescope, built in 1994, was originally tasked to measure the Earth's orientation and motion of its rotation axis. After its shut down in 2000, the telescope is now being used as part of the SkyNet telescope project at the University of North Carolina at Chapel Hill. The telescope is also used to test a PAF system to be eventually used on the Green Bank Telescope. The PAFs promise the capability to look at the more sky area for faster surveys, providing a greater field of view and better canceling of radio frequency interference. The phased array feed project called the FLAG project, is in collaboration with Radio Astronomy Systems Research group at Brigham Young University, who performed the first experiments in Summer, 2008 with a 19-element single polarized dipole array.

4.5.2   Experimental Setup

The experiments were conducted on the 20-meter in two phases - January, 2011 and April, 2011. The most of the experimental setup was done by the telescope staff, under the supervision of Roger Norrod and Dr. Rick Fisher. All the phased array feeds - single polarized room temperature array, dual polarized room temperature array and dual polarized cryo-cooled array, along with the receiver boards and the LO power distribution - were shipped to the observatory, and were installed on the dish and into the front-end box by the observatory staff. The observatory has developed their own 40-channel data acquisition system using 10 rack mount computers, which was used for taking data during the experiments. The other setup involved installation of a fiber-optic link between the dish and the control room.

4.5.3   Observation & Data Taking

The first phase of observations took place from January 23, 2011 to March 14, 2011. and the second phase of observation took from April 14, 2011 to May 23, 2011. Since the observatory's data acquisition was used for all data taking operations. Most of the observations were mostly done remotely and with the help of Anish Roshi, software engineer at observatory. All the data was stored on external hard drives and the hard drives were shipped to BYU. The observation took place according to the planned observation schedule.

Here is a summarized list of all the experiments done:

- A fine grid of 23x23 pointings on a bright point source with high flux density at center of frequency of operation.

- Frequency scan grids of 3x3 pointings over 1 GHz to 2 GHz in 20 MHz steps to compute sensitivity of the feed across the band.

- Calibration grids taken at multiple times in a day for a number of days to collect far field and rim calibration data sets to analyze the far field calibration vectors and the possibility of updating stale calibrators using rim calibration data.

- Fine grids at different frequencies in range of 1 GHz to 2 GHz to analyze the change in beam pattern with frequency.

- Slice cuts on weak sources with each set of calibrator to image and observe the degradation in calibration.

- Coarse grid at the beginning of each calibration using the vertex antenna in burst mode to obtain a phase reference for each calibrator in the grid to measure the phase pattern.

- Fine cross-elevation cuts over calibration sources to determine best position for an off pointing relative to the source.

4.5.4   Experimental Results

(a) Boresight image of the calibration source   (b) Image of the weak source
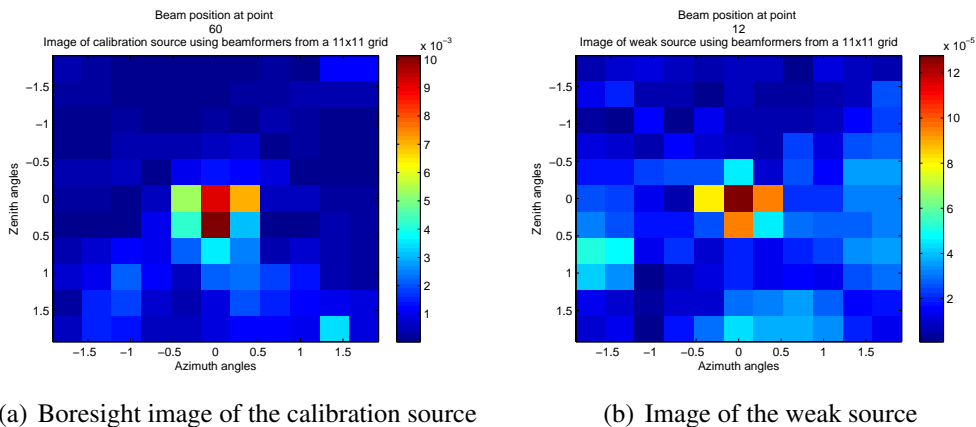
Figure 4.12: Figure (a) shows the boresight image of the calibration source formed using calibration data, and (b) shows the image of weak source formed using the weak source and the beamformer weights calculated from the calibration source data.

The data obtained from the weak source observation was analyzed. Figure 4.12 shows the image of calibration sources and weak source. The images are formed using the process discussed above in Sec.4.2. The weak source can be seen in the image shown as the images are formed at different pointings of the slice, the source can be seen at different positions, but there is also a lot of noise in the image. In comparison between the two images of the calibration source and the weak source, the noise difference can be seen despite using the same beamformer coefficients for forming both the images. This suggests that the noise floor in both the images was not equal.
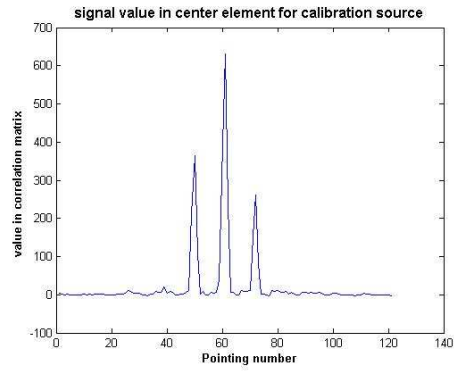
Figure 4.13: Figure shows the value of the $\mathbf{R}_s(1,1)$ for the calibration source.
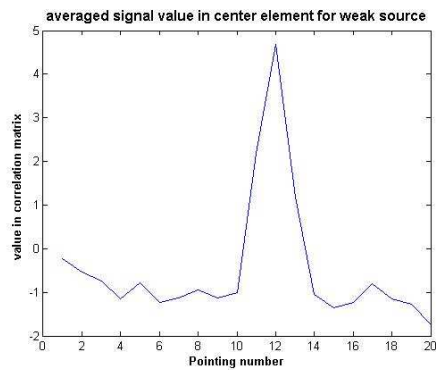
Figure 4.14: Figure shows the value of the $\mathbf{R}_s(1,1)$ for the weak source. Both the plots are formed by subtracting the $\mathbf{R}_{\text{off}}$ correlation matrix obtained from the off pointing from the $\mathbf{R}_{\text{on}}$ correlation matrix for the on pointings.
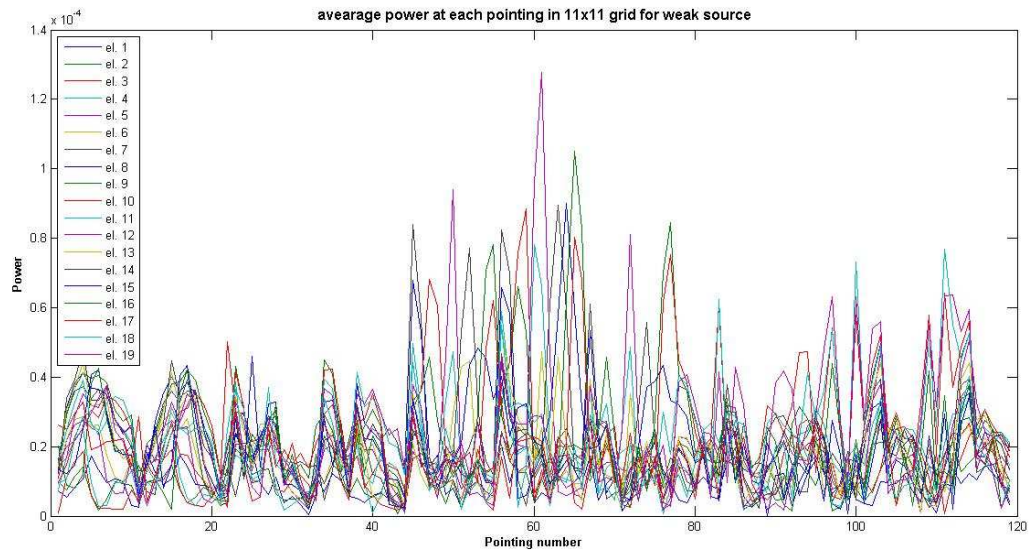
Figure 4.15: Figure shows the power of the weak source observed in the all the elements of the array for all the pointings.
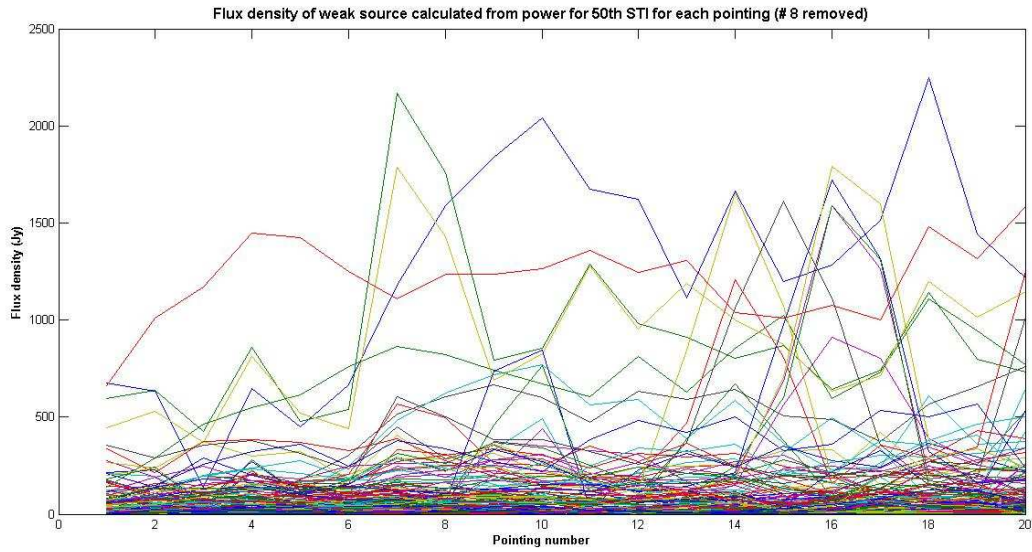
Figure 4.16: Figure shows the flux density calculated from the power in all the array elements for all the pointings in the grid.
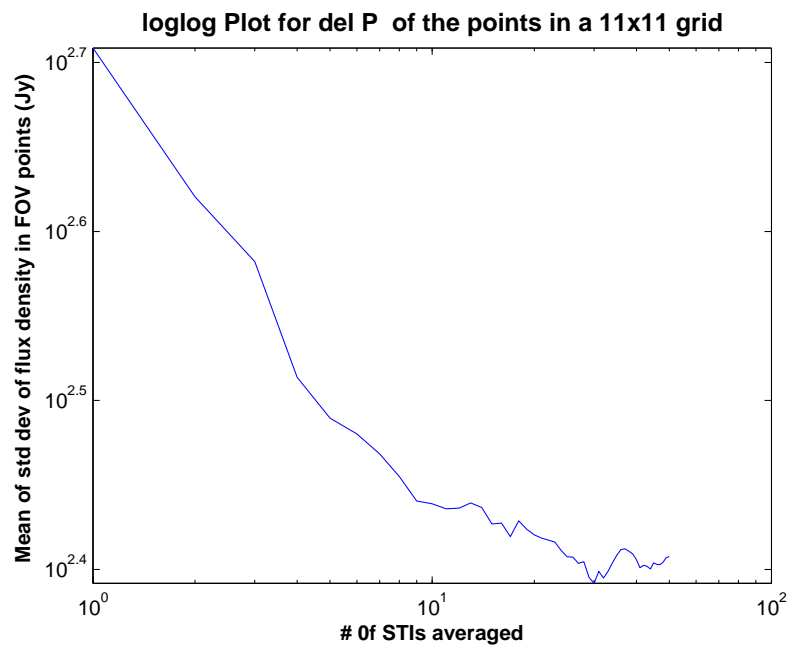
Figure 4.17: Figure shows the logarithmic plot of the standard deviation of the noise over increasing number of STIs.
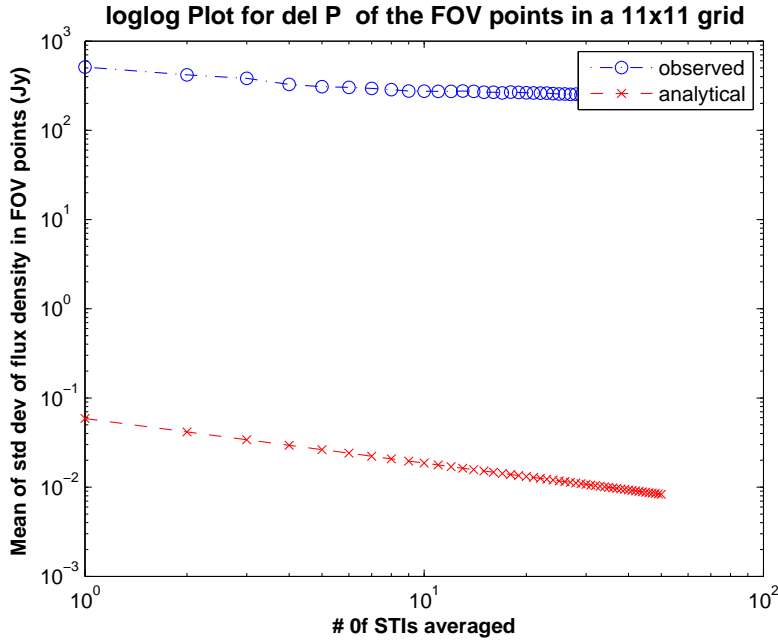
Figure 4.18: Figure shows the comparison between the logarithmic plot of the standard deviation of the noise over increasing number of STIs and the analytical noise field.

To analyze this noise floor difference in two images, the variation in the noise floor in the image was studied. Figure 4.13 and figure 4.14 shows the net signal value in correlation matrix of the calibration source and the weak source respectively. The net signal value is calculated using Eq. (4.1). This difference in the two matrices is mainly due to the difference in the flux density of two sources. The noise behavior in the image of the weak source was further studied using the analysis given in the section 4.3.

Figure 4.17 shows the variation in the power in noise only grid points in terms of standard deviation over the data accumulation period which is denoted by the number of STIs. The plot shows that the average noise decreases as the number of STIs increase. Figure 4.18 shows the comparison between the standard deviation of the power in the noise floor with that of the analytical noise power given by the Eq. (4.9). The observed noise was much higher than the analytical. This leads to the fact that the noise floor varies more rapidly than and the level is much higher. It was also observed that the net signal value also depended on the off pointing used for the calculation.

4.6 Conclusion

This chapter discussed the experimental results obtained from the experiments done at the Arecibo and a part of the experiments done at Green Bank, WV. The results from the feasibility study conducted for the design of the PAFs for the Arecibo Observatory are discussed. The sensitivity of the array at different positions is shown, and the problems associated with them are discussed. The data was also taken to find other characteristics of the PAFs.

The experiments at Green Bank Observatory, WV, provided data for analysis of many issues associated with the feasibility of the PAFs on radio telescopes. One of the issue is to image the weak sources with PAFs. The images were formed using the observed data from various weak sources, but the images have high noise content in them since the two sources have different flux density and noise levels. The problems associated with the imaging is also discussed.

Chapter 5

The Real-Time Digital Backend

5.1   Introduction

This chapter discusses the development of a field programmable gate array (FPGA) based PAF digital back-end system using hardware from the Center for Astronomy Signal Processing and Electronics Research (CASPER) for a real-time correlator/ beamformer from a PC-based system performing correlator and beamformer in post-processing. The earlier system consisted of a hub computer and five rack-mount terminal computers having ADLINK Analog-to-Digital cards. The processed data from the cards was stored on the terminal computers, and was later aggregated and correlated for post-processing and analysis. The hub computer controlled the data taking process and also the communication between the terminal computers and the telescope control computer.

The new system uses a 64-channel analog to digital card (ADC) sampling at 50 Msamples/sec, which is connected to an FPGA board for real-time processing of the signals and streaming this processed data over 10 Gigabit Ethernet (10 GbE) connection to a server or to a Power PC over 100 Mbits/s switch. This system provides usable bandwidth of 20 MHz per input, in comparison to 425 kHz usable bandwidth of the older system. The ultimate goal is to have a system with 300 MHz bandwidth for PAFs on the Arecibo or the Green Bank Telescope (GBT). This back end will also support a millimeter wave PAF in development at the University of Massachusetts (UMASS) and as an digital backend for phased array feed at the GBT.

The system will ultimately consist of a frequency channelizer (F-Engine), correlator (X-Engine) and a beamformer (B-Engine), each with its own dedicated FPGA board. The current system status and future development will be discussed in detail in this chapter.

5.1.1 CASPER Collaboration

The CASPER group at the University of California, Berkeley, has developed a common platform for digital backend for radio astronomy systems using reconfigurable hardware. The center has now become an international collaboration with the support from many research organizations and universities from around the world.

The aim of the CASPER program is to allow astronomers to rapidly design and deploy new instruments by developing a real-time streaming application specific hardware with much greater simplicity in design which uses parametrized, platform-independent gateware libraries that can be run on reconfigurable, modular hardware building blocks. The digital hardware design process is simplified to a great extent by providing a graphical interface to FPGA firmware development using MathWorks Simulink. It provides customized hardware block libraries to be used with XILINX System Generator Tools library. This relieves the user from having to master the VHDL skills to design digital systems. CASPER also provides different kinds of ADC and FPGA boards to interface with the CASPER toolflow.

5.1.2 BYU-CASPER Collaboration

The BYU-Radio Astronomy System (BYU-RAS) Research Group began its collaboration with the CASPER in January, 2010. From January, 2010 to July, 2010, Dr. Baker and Dr. Parsons at UC Berkeley sponsored Jonathan Landon, a graduate student at BYU, as a visiting student researcher to learn the CASPER toolflow [18]. He helped in maintaining the Precision Array for Probing the Epoch of Reionization (PAPER) correlator, and installing it at Green Bank, West Virginia. The BYU-RAS group has four Reconfigurable Open Architecture Computing Hardware (ROACH) boards, four iADC and two x64ADC cards, 64-input ADC cards. He also started initial tests using x64adc to begin CASPER-based digital backend.

5.2 System Overview

This section will discuss the different parts of the digital backend in detail. The BYU-RAS digital backend hardware consists of four ROACH boards with two x64ADC boards and four iADC
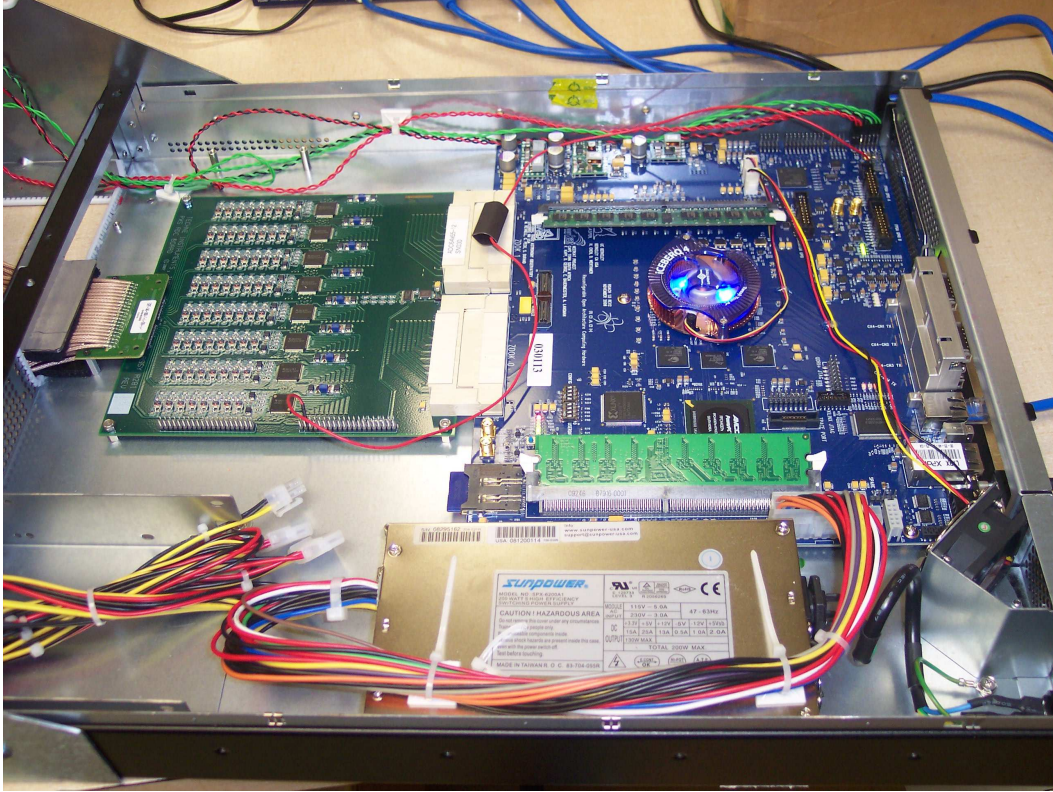
Figure 5.1: A close up view of ROACH board and x64 ADC card.

boards, a server computer for data storage and compiling the designs and a host computer for the boards.

5.2.1 Virtex-5.0 FPGA-based ROACH Board

ROACH is a standalone XILINX Virtex-5 FPGA based processing board [19]. It has 10 Gigabit Attachment Unit Interface (XAUI) / 10 Gigabit Ethernet (10GbE) / 4 port XAUI (CX4) interfaces from both the Interconnect Break-out Board (IBOB) and Berkeley Emulation Engine (BEE2) platforms, with Z-DOK interface of the IBOB with the high capacity Dynamic random-access memory (DRAM) memory and the usage model of the BEE2. A separate Power PC running Linux is used to control the board and allowing interfacing between the software registers, Block random-access memory (BRAM), First-In First-Out (FIFOs) on the FPGA with the external devices over Ethernet. Figure 5.1 shows a single ROACH board connected to a x64ADC board.

49
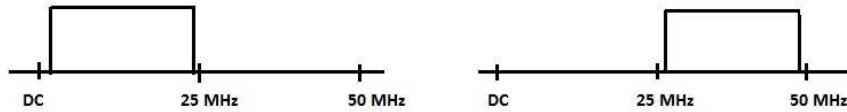
Figure 5.2: A block diagram showing two subsampling bandwidths.

The ROACH board has two quad data rate static random-access memory (SRAMs) which provide high speed, medium capacity memory and one double data rate synchronous dynamic random-access memory dual in-line memory module (DDR2 DIMM) providing slower-speed high-capacity memory for the FPGA. Two Z-DOK connectors on the board allow interfacing with the ADC boards just like an IBOB. Four CX4 connectors can be used to connect ROACH boards together or with other devices having XAUI/ 10GbE interfaces, providing a total bandwidth of 40 Gbits/sec.

5.2.2 x64 ADC Board

The x64ADC board has 64 input channels with 12-bit sampling [20]. Each board has eight ADC chips, each sampling eight independent input channels at 50 Msamples/sec. The analog receiver boards set the final IF bandwidth between 27.5 MHz to 47.5 MHz. The ADC board has a capacitor after a balun transistor which converts a single-sided values to differential pairs and does anti-alias filtering. This capacitor was removed from the board to enable baseband subsampling techniques. The two sub-sampling bands are shown in Figure 5.2.

5.2.3 System Description

Figure 5.1 shows an interior view of the BYU ROACH board with x64 ADC card on the left and the FPGA board on the right side. The FPGA is located under the fan as shown in the figure. The board also has a Power PC, running a modified Linux operating system version, borph, which make interactions with the FPGA easier. The memory registers in the FPGA appear as files in the Linux. The far left side of the image shows an coaxial cable assembly with 80-pin QSE/QTY connector on one side mounting to the x64 ADC board and 80 SMA connectors on the other side.

Figure 5.3: Image showing the front view of all the ROACH boards. The bottom ROACH board shows the front panel of the board having the inputs for the x64 ADC.

Figure 5.3 shows the front panel of the ROACH board with SMA connectors. These connectors provide input to x64 ADC card on the ROACH board. The figure also shows the other ROACH boards which will be used for implementing the other stages in the system including beamformer and correlator.

5.3 Initial Setups

Figure 5.4 shows an instrument rack with the ROACH board and x64 ADC card, another ROACH board for further development, a host computer for the ROACH boards and a server system. The ROACH boards and x64 ADC cards were discussed in the previous section. The server system is used for gateware designs. It has all the required CASPER libraries installed on it. The server system runs a 64-bit RHEL5 operating system and MATLAB R2009a, alongwith XILINX ISE 11.4. Designs are created, simulated and compiled using Simulink. Once the designs are simulated, they are compiled using a pre-supplied wrapper code called bee_xps from the CASPER

Figure 5.4: A view of the instrument rack with ROACH boards, a host computer and a server computer.

library. This wrapper creates a .bit and .bof files for the designs. The .bof file, transferred to the ROACH board file-system, is used to program the FPGA.

The host computer runs Ubuntu operating system and is used to interact with the ROACH boards. This system also handles the boot files and the file system for the ROACH boards. All the ROACH boards have been assigned IP addresses using a DHCP server on the host and are set up to look to this host for booting and their file system, to allow all the ROACH boards to use a common file system. To interact with the ROACH, control scripts are run remotely by logging into the ROACH system over a SSH or telnet connection over 100 Base-T Ethernet connection. The .bof files are also stored on this host for the ROACH to program. The .bof file runs as a program on the ROACH and allot different registers and memory needed for the program, which is much easier than using a JTAG programmer to program the ROACH board.

The server computer has a 10 GbE connection, which makes it useful to receive and write the 10 GbE packets to the hard drives on server and store them. Since it has only one connection, the data transfer or writing speed is limited. For the full 64 channel system operation at full designed speed, the server will be replaced by a rack of computers with multiple 10 GbE connections to write the data at such a high rate.

5.4   Back End Development

The initial goals for the digital back-end was to have a replacement for the 40-channel data acquisition system with the data streaming over 10 GbE connection and data storage on the terminal computers. This provided us with three main objectives: to develop a narrow band real-time spectrometer for at least 40 channels, a real-time beamformer, and data streaming and storing data in the terminal computers for post-processing.

Currently, the system demonstrate a real-time spectrometer and data streaming for a selective number of frequency channels with streaming to a terminal computer over the 10 GbE connection. The process of verifying the data send and received is still under progress. The RAS group is also building up a beamformer, using VHDL coding instead of Simulink. The initial simulations and tests have been done, but the design is still required to be tested with the integrated system. All these three parts are discussed in detail in the following subsections.

5.4.1 64-channel Spectrometer

Figure 5.5 shows a block diagram of real-time spectrometer. The system shown in the figure does a power accumulation over each frequency channel of the spectrum, and then transfers the accumulated data forming the packets for a group of specifically chosen frequency channels over a 10 GbE connection to a terminal computer.

The spectrometer takes 12 bit signed values as input from x64 ADC card. There are four channels coming out serially on each x64 ADC input. The polyphase filter bank (PFB) block [21] requires a complex input, so two ADC inputs are combined using a XILINX real-to-complex (ri-to-c) block, which make it a complex input for the PFB block. The output coming from the PFB block is just a delayed filtered version of the inputs. The PFB block uses four taps from a hamming window where each tap is delayed by a fixed number of clock cycles. Here the taps are delayed by 0, 1*NFFT, 2*NFFT, 3*NFFT, where NFFT is the total number of desired frequency channels. As the outputs come out from the PFB block, they are again separated back into two real streams using a XILINX complex-to-real (c-to-ri) block.

Since each ADC input has four channels serially coming out and FFT requires to see all the NFFT time samples for a particular channel one after another, it becomes necessary to rearrange the data. This function is performed by the reorder block. The reorder block rearranges the data such that it captures 4*NFFT time samples and rearrange them so that all the time samples for the first channel come out first, followed by second and so on and then the process repeats.

The outputs from the reorder block are then fed in the FFT block. This block is called fft_biplex_real_2x block [22]. It takes real input and gives out complex output. The frequency channels coming out from the block are only positive ones, the block itself rejects the negative frequency channels, thus making only half of the NFFT channels available at the output. All the blocks have a sync clock going in and out which helps in determining the validity of the data. For the purpose of beamforming and correlation, this output from the FFT can be used directly.

For the spectrometer, we perform a power accumulation for each frequency channel. The power is calculated from the output of the FFT and is quantized and accumulated for a larger period of time and the values are stored in the BRAM. The values are then read over a 100 Base-T Ethernet connection from a host computer using a python script and the spectrum is plotted. The spectrum can also be made to animate for every iteration using a modified python script. One issue
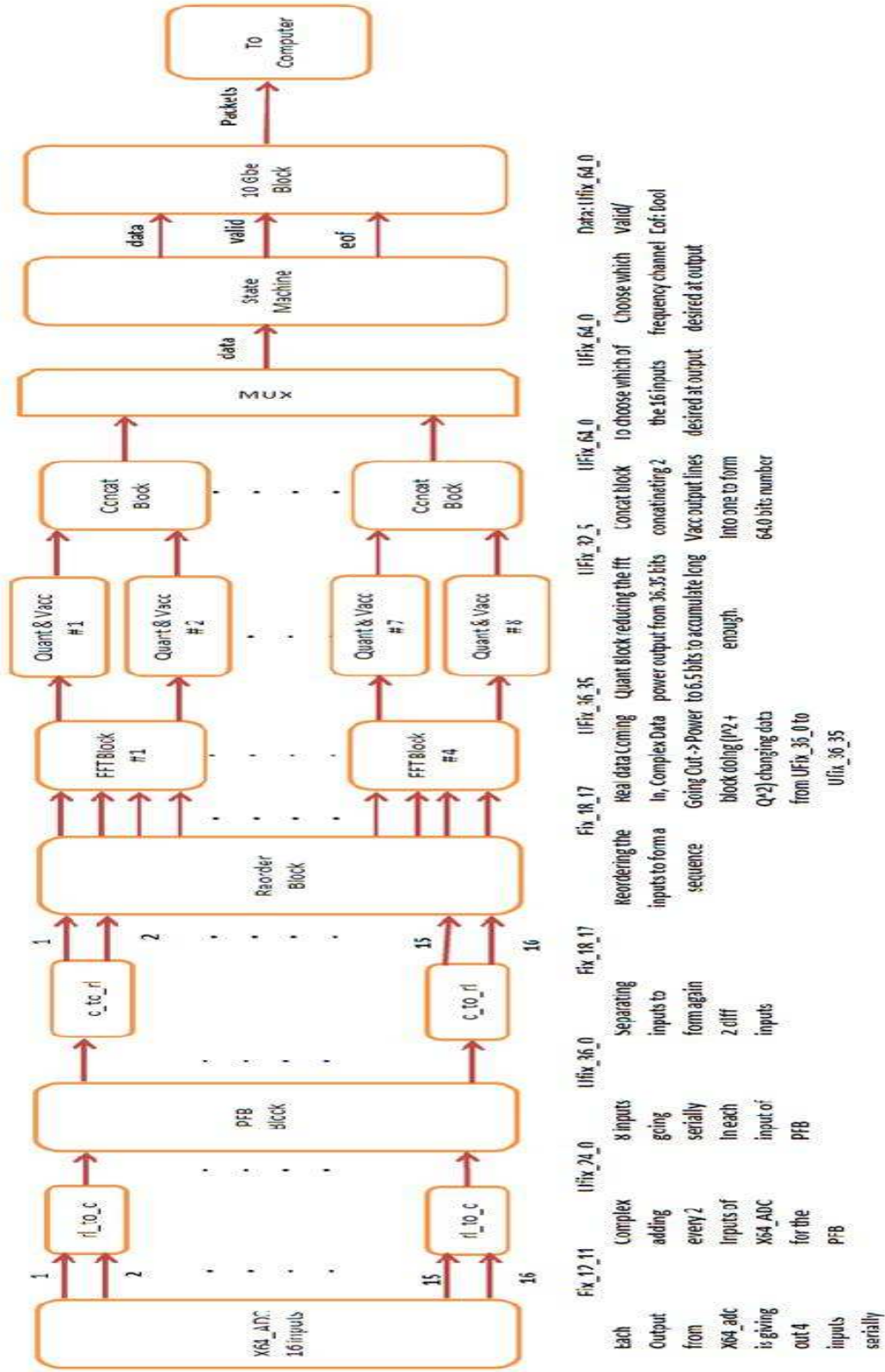
Figure 5.5: The block diagram of a real-time spectrometer, doing frequency channelization, quantization and accumulation of data and then transferring data over a 10 GbE connection for a specific number of frequency channels.

with this using python over is that the update rate is slow in compare to the accumulation length, so to plot the spectrum properly, the accumulation rate should be kept much higher.

5.4.2   10-GbE Interface

The 10 GbE ports have much faster data transfer rate in comparison to 100 Base-T ports. Since the data is needed for post-processing, it become necessary to use these 10 GbE ports for transferring the data. Due to the limited size of the BRAMs, it was difficult to check the system over a longer range of data. The 10 GbE ports are used mainly for following purposes.

The 10 GbE ports are used for streaming raw samples directly from the ADC to the terminal computers. This was done to understand the ADC behavior and the synchronization in between the channels and the ADC chips. The limiting factor in doing this is the disk write speed. The rate at which data is coming out from the FPGA is 4.8 GB/sec (38.4 Gbits/sec) which is much faster [18]. Thus, a reduced bandwidth was required to write this data to the disks on the terminal computer.

The 10 GbE ports are also used for streaming the complex data coming out from FFT block to the disks for the post processing of the data. The disk write speed is also a limiting factor for this process. Since there are multiple antennas output coming at the same clock cycle from the FFT blocks, a separate header containing the information about the antennas and the frequency channel, is created and inserted before every 10 GbE packet, so the data can be arranged correctly at the terminal computers. This function is performed by a state machine block, as shown in Figure 5.5. The state machine is also used to select a group of frequency channels which form the band of interest. This helps in reducing the bandwidth required for writing the data to disks on terminal computer.

5.4.3   Beamformer Status

A hardware-based beamformer is in the building process. The beamformer takes the frequency channelized data coming out from the FFT block, multiplies them with the appropriate beamformer coefficients and add them to form a beams. The ultimate goal is to form forty beams using all the 64 input channels. The beamformer is implemented as a black box, in order to make it usable in Simulink. The black box contains codes written in Verilog Hardware Definition Language (VHDL).

56

The beamformer coefficients are stored in the memory on the ROACH. Since a different channel requires a different beamformer coefficient for different frequency channel, the VHDL code updates these coefficients in accordance with the frequency channel and make them available to the multipliers. The multipliers are DSP48 slices and blocks to perform the multiplication.

The beamformer forming only one beam, works in simulation and is tested using iSIM, and is currently being tested with the ROACH hardware. This will be later expanded to form at least seven beams.

5.4.4 Contributions

Since this project has been a joint effort and always involved more than one student on the project, in this section I am describing all the contributions made by me towards the project. Here are my contributions to the development of the back end system.

- Getting familiar with the CASPER toolflow and going through a steep learning curve to learn more about the system.

- Initial setup of the CASPER system which involved arranging all the hardware required for the toolflow setup and installation of the softwares on the computers.

- Identifying all the inputs corresponding to a x64 ADC card and verifying their response to the input signal using a design and a python script written to plot all or a single channel at a time.

- Manually removing all the capacitors after the balun transistors from all the channels on x64 ADC card to enable baseband sub-sampling techniques using the ADC board.

- Designing a full 64-channel spectrometer. This spectrometer was able to perform a spectrometer by accumulating all 64 frequency channels coming out from the F-engine and storing the values in BRAMs on the ROACH board and then reading them over a 100 Base-T Ethernet connection with a Power PC and doing an animated plot for all the channels using a python script.

- Making a customized state machine block using XILINX blocks for use with the 10 GbE interface. This block was designed to select a particular frequency channel or a number of frequency channels to reduce the data rate over the 10 GbE interface.

- Verification of the cross coupling between different channels on the x64 ADC card.

- Streaming raw samples directly from the x64 ADC outputs to the terminal computer using a single 10 GbE interface. The data rate was found to be too high for the computers to write and the packets were found to be missing.

- Making the use of 10 GbE interface in the spectrometer design to enable the BRAM data to be send over the 10 GbE interface and storing that data on terminal computers for post-processing.

- Designing a hardware based correlator using the initial setup from the CASPER community and modifying it according to the x64 ADC use.

  Other parallel efforts involved:

- Setting up two additional CASPER toolflow systems with a server computer and a host computer for designing and talking to the ROACH boards respectively. These systems were used by the senior project groups for compiling and running their designs on ROACH boards.

- Helped a senior project group with the beamformer development on making the students familiar with the F-engine functionality and its working, which is used as an input to the beamformer B-engine. I also wrote the scripts for the beamformer to read the BRAMs which stores the final accumulated outputs of the beamformer.

- Helped another senior project group working on making a 4-channel 800 MHz spectrometer using two iADC cards. This involved making them familiar with the iADC cards and its operation, helping them in doing tutorials, setting up the signal generators for multiple channel use.
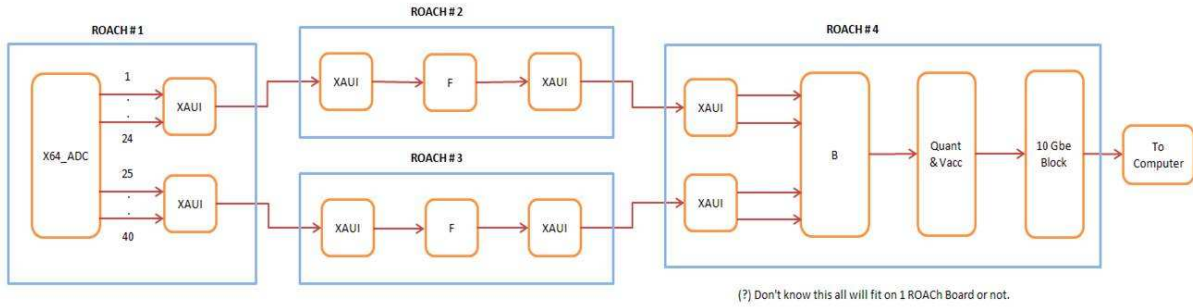
Figure 5.6: A possible architecture for the digital backend system using four ROACH boards. The first ROACH board sends samples to the ROACH 2 and ROACH 3 which performs the F-engine on data. This frequency channelized data from both the boards is send to ROACH 4 which then performs the B-engine operation and streams the data to a computer using a 10 GbE port.

Figure 5.7: Another possible architecture for the digital backend system using three ROACH boards. The first ROACH board performs F-engine operation on half of the channels and sends the samples for the other half input channels to ROACH 2 which does a F-engine on it. The frequency channelized data from both of these boards is collected by the ROACH 3 which does a beamforming on it and send the accumulated data to a computer over a 10 GbE port.

5.5   Future Development

5.5.1   Beamformer Development

The current beamformer design has not been tested with the hardware. It will be of great benefit to know how it works, and how efficiently it updates the coefficients and the behavior of multipliers. The analysis and testing of this design will decide on the architecture to use. There are three different possible architectures, which are explained below in detail.
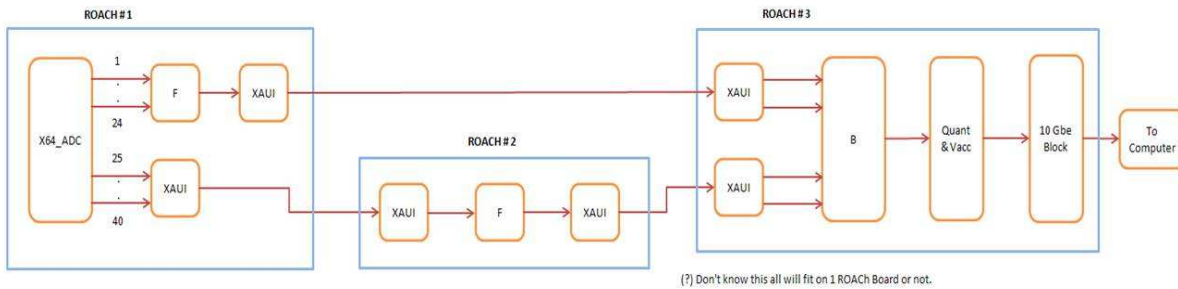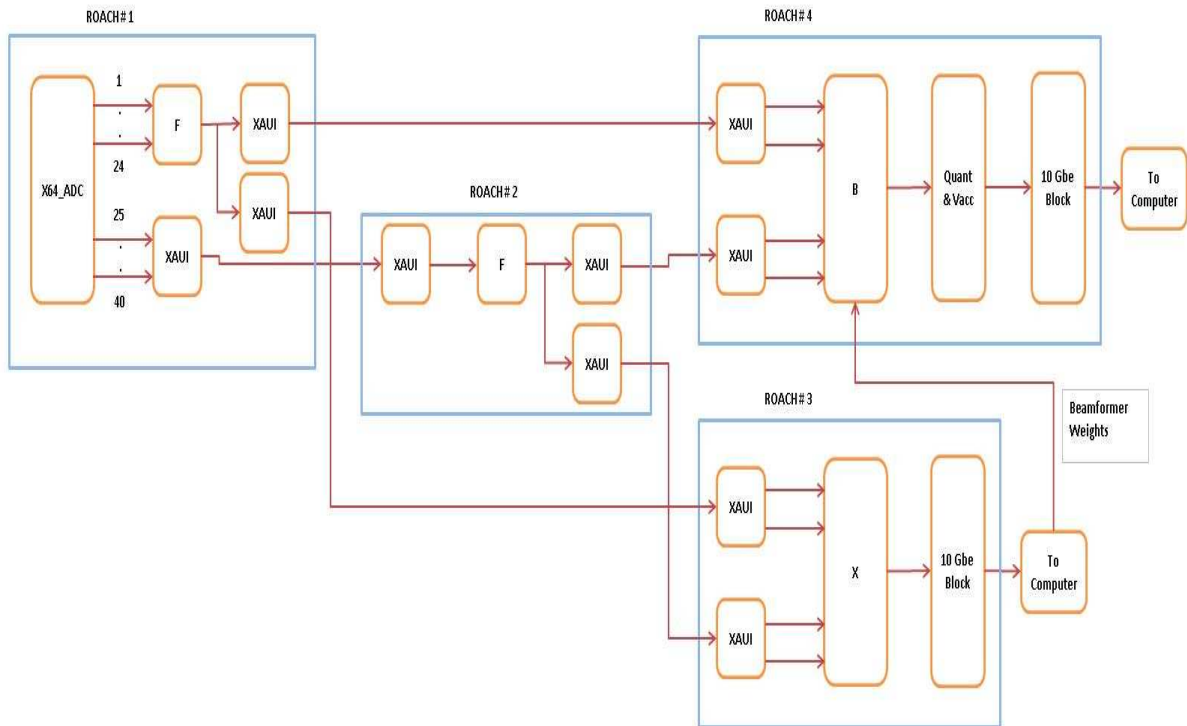
Figure 5.8: An architecture for the digital backend system using four ROACH boards. The first ROACH board performs F-engine operation on half of the input channels and send the samples for the other half input channels to ROACH 2 which does a F-engine on it. The data from both of these is provided to ROACH 3 and ROACH 4. ROACH 3 performs the correlator function and stores the matrices on the a computer. ROACH 4 performs the beamformer function and stores the accumulated data on a terminal computer.

Figure 5.6 shows an architecture with F-engine and B-engine using total of four ROACH boards. The boards use XAUI interface to transfer data between the boards and 10 GbE interface to transfer data to the terminal computer. ROACH 1 is programmed to take signal from x64 ADC and form packets, which are then transmitted over to the ROACH 2 and ROACH 3 boards over four XAUI interface. Half of the input channels are transmitted to ROACH 2 and the rest of the channels are transmitted to ROACH 3. ROACH 2 and ROACH 3 are implemented to do F-engine. These boards receive packets from the ROACH 1 board over XAUI interface, de-packetize the packets and arrange them and do F-engine operations on them. The frequency channelized data from the F-engine is send to ROACH 4 which does the beamforming. The packets are formed on both ROACH 2 and ROACH 3 boards and are send to the ROACH 4. The packets received from both the boards are de-packetized and arranged to provide an input for the B-engine. ROACH 4

performs the beamforming operation and the outputs are accumulated over period of time using a vector accumulator and then the packets formed are transmitted to the terminal computer over a 10 GbE interface. The terminal computer stores the packets received using a script written in C and using a "gulp" software, which reads and removes the header from the packets and arranges and stores the data into a specific format, which can be used for post processing or plotting the results from the beamformer.

Figure 5.7 shows another architecture with F-engine and B-engine using total of three ROACH boards. This architecture also uses XAUI interface to transfer data between the boards and 10 GbE interface to transfer data to the terminal computer. ROACH 1 is programmed to take signal from half of the inputs of x64 ADC and form packets, which are then transmitted over to the ROACH 2 using two of the XAUI interface. The second half of the input channels are processed through the F-engine and their frequency channelized inputs are then transmitted to ROACH 3. ROACH 2 implement the F-engine on the rest of the channels using data it received over two XAUI ports. This board receives packets from the ROACH 1 board over XAUI interface, de-packetize the packets and arrange the data to perform F-engine operations on them. The frequency channelized data from the F-engine is send to ROACH 3 which does the beamforming. The packets from both ROACH 1 and ROACH 2 boards are received by ROACH 4 which de-packetize them and arrange the data to provide an input for the B-engine. ROACH 3 performs the beamforming operation and the accumulated outputs over a period of time are done using a vector accumulator and then the packets formed are transmitted to the terminal computer over a 10 GbE interface where they are stored after removing the header from the packets. It also arranges and stores the data into a specific format, which can be used for further either post-processing or plotting the data in real-time.

Figure 5.8 shows an architecture with F-engine, X-engine and B-engine using ROACH boards. ROACH 1 takes data from x64 ADC board and applies a partial F-engine to half of the channels. The rest of the channels data is send in form of packets over XAUI interface to ROACH 2, which applies F-engine operation on the rest of the channels. The frequency channelized data from both ROACH 1 and ROACH 2 is packetized and the packets are send over XAUI to both ROACH 3 and ROACH 4. ROACH 3 depacketizes the packets and arrange data in to the format for the correlator. ROACH 3 performs the correlator function of creating a matrix of all pairs of

antennas inputs for each frequency channel. A matrix is formed by multiplying all antenna inputs and accumulated. The output of the correlator is send over the 10 GbE interface to the control computer which depacketizes the packets and store the correlation matrix. The control computer also computes the sets of beamformer weight coefficients for the beamformer implemented on ROACH 4. These beamformer weight coefficients are written to a BRAM on ROACH 4, which use it for multiplying to the frequency channelized data obtained form ROACH 2. ROACH 4 performs the beamforming operation of multiplication of coefficients and the data for each of the frequency channel and the result is accumulated using a vector accumulator. This accumulated data is then stored on the terminal computers using a 10 GbE interface. The stored data can either be used for plotting the beams in real-time or for post-processing.

5.5.2 64-channel Hardware Correlator

The hardware correlator design for the PAFs is based on the CASPER X-engine design made for the Medicina group in Italy [23] using the x64 ADC having 32 single polarization inputs and processing 40MHz bandwidth with a usable 16MHz bandwidth centered at sky frequency of 408MHz at an IF of 40MHz. The design uses a total of two ROACH boards, one for the F-engine and the other for the X-engine. Correlation is a process of creating a matrix for each frequency channel by multiplying all pairs of antenna channels and accumulating over time. The complex multiplication of these antenna pairs is done using the XILINX multipliers, which are limited on resources present on each ROACH board. The correlator design uses a clever way of utilizing these multipliers so that the whole design fits on one ROACH board. For a large number of frequency channels, the design can be easily spread over a number of ROACH boards which perform correlator function on the data received from the F-engine ROACH board over XAUI interface. The design is currently in process of being modified as per the needs of the PAFs.

The matrices produced by the X-engine can be used for calibration purposes in either real-time by calculating the beamformer coefficient weight vectors from the correlation matrices and transmitting them to the B-engine, or can be stored for post-correlation beamformer application for beamformer modification and interference mitigation. Since the beamformer coefficients are needed to be calculated only once, the board can be used for a period of time and then reprogrammed to perform some other operation. For the post-correlation beamformer application, the

packets are streamed to the computer over a 10 GbE interface and all the packets are provided with a particular header information which helps to identify and arrange according to the antenna outputs and frequency channels contained in the packet.

5.5.3 Conclusion

The digital backend hardware development at BYU and future development steps required were covered in this chapter. The architectures possible for the system were also discussed in the chapter. The final system will make the current data acquisition system expanded to 20 MHz bandwidth and the number of antennas increased to 64 channels with the capability of real-time analysis of data. Though the progress for the system development has been slow with the simplified world of CASPER where most of the signal processing blocks are available through the international collaborators, it was worth putting the time into the development as the process involves a steep learning curve. With the addition of each new block into the design to do the further processing, it involves the timing and logic verifications at every step in the design for the compilations to complete.

An initial time of four months was spend on setting the whole system and the server and the host computer and developing a full 64-channel spectrometer doing a plot of the spectrum. A lot of time after that was spend on getting the data produced from the spectrometer stream to disk over 10 GbE interface working, writing a code for the terminal computer to receive packets and write them to disk in a proper format and verifying the data stream to disk. In future work, a major effort will also be required to write a script to make the system useful for the real-time science and astronomical applications.

Chapter 6

Conclusions and Future Work

6.1   Conclusions

This thesis discussed contributions to the Radio Astronomy group at BYU in developing new analog down-converter receiver boards and setting up a new real-time digital data acquisition system. The development of new receiver boards upgraded the system to 40 input channels from the previous 20 input channels, having the same bandwidth of 425 kHz and sampling at 1.25 Msamples/sec to stream data to disk for post-processing. Since the IF filter was placed on the same receiver board, the receiver boards size were much smaller. Each board had four channels implemented on it. The cross coupling between different channels on the same board was at least greater than -40 dB, which was found to be better than the previous receiver boxes. The noise figure was found to be lower than the previous receiver boxes. The receiver boards were used in the phased array feed experiments at the Arecibo Observatory, Puerto Rico and the experiments at the 20 meter dish in Green Bank, WV. All the boards were found to be stable and performed as required for all the observations.

The thesis also discussed the initial results from the experiments done at Arecibo observatory for the feasibility of the PAFs on their 300-meter dish and the experiments done at 20-meter dish located in Green Bank, WV. The noise floor leveling problem found from the analysis of weak source needs to be analyzed in more detail.

The development of new real-time digital backend for the phased array feeds has involved a steep learning curve. Still, much progress has been made in developing a real-time 64 channel spectrometer which can have up to 256 frequency channels and generate animated plots updating according to the length of acquisition time. An effort has also been made to develop a beamformer which uses a F-engine from the spectrometer design and a B-engine to beamform the frequency channelized data. A 10 GbE interface between the ROACH and a terminal computer to transfer and

store the data packets from ROACH for doing post-processing and applying a software correlator has been built. Since the data rate is too high for the computer to write the packets, the data rate was reduced by choosing only a few of the frequency channels using a state machine, and transferring and storing the data for these frequency channels.

6.2   Future Work

Expanding the array from single-polarization feed to dual-polarization feeds and having increased bandwidth and sensitivity are the main points of focus of future phased array feeds for the radio telescopes.The long term goal is to enable science observations with phased array feeds. The increase in bandwidth of operation and the further increase in number of input channels sets the requirement of the system to build a new down-converter receiver card. The new receiver cards will have increased bandwidth of 20 MHz. This receiver will have a new IF filter having the required bandwidth of 20 MHz and a different SAW filter. The new receiver cards will operate in range of 27.5 MHZ to 47.5 MHz. The design of these receiver boards have been done and a prototype is being made and tested for cross coupling, noise figure and other parameters. These new receiver cards will be tested with the full system in experiments at Green Bank, WV in Spring, 2012.

The future work in developing a real-time digital backend for phased array feeds involves developing a full 20 MHz bandwidth correlator and beamformer as an initial step towards the goal of developing a full 300 MHz bandwidth 64 channels digital backend system. Though it is still not clear about a better system with a FPGA based system approach or with a GPU based system approach. Staying with this FPGA based approach, the primary goal should be able to send all the spectrometer data over 10 GbE interface to a number of computers using a 10 GbE network switch. Next step can be to develop a B-engine forming a number of beams using a number of ROACH boards and streaming the data to store on the computers. Currently the beamformer coefficients are programmed into the BRAM while compiling the design, but an interface can be added to change or update the beamformer coefficients while the design is in use to provide more flexibility to the observations. Another approach can be to develop a FX-engine with a frequency channelizer and correlator using a number of ROACH boards. There may be a scope of changing the designs to utilize the FPGA resources in a better way and making the designs more efficient. There is a trade-

off associated with the number of antenna inputs and frequency channels - to get a finer frequency resolution, the number of inputs can be reduced from 64 to 40 input channels for the current system in the design to make better utilization of BRAMs and resources present on a FPGA board. Also, keeping the track of recent developments and the challenges faced by the CASPER community will help the development process going on at BYU.

Bibliography

[1] H. Cortes, "Personal Communication," 2010.

[2] J. D. Kraus, *Radio Astronomy, Second Ed.* Powell, Ohio: Cygnus-Quasar Books, 1986.

[3] B. Jeffs, K. Warnick, J. Landon, J. Waldron, D. Jones, J. Fisher, and R. Norrod, "Signal processing for phased array feeds in radio astronomical telescopes," *Selected Topics in Signal Processing, IEEE Journal of*, vol. 2, no. 5, pp. 635 –646, oct. 2008.

[4] L. Staveley-Smith, W. E. Wilson, T. S. Bird, M. J. Disney, R. D. Ekers, and K. C. Freeman, "The Parkes 21-cm multibeam receiver," *Publications of the Astronomical Society of Australia*, vol. 13, p. 243, 1996.

[5] H. Rottgering, "LOFAR, a new low frequency radio telescope," *New Astronomy Reviews*, vol. 47, no. 2, pp. 405–409, September 2003.

[6] D. DeBoer, W. J. Welch, J. Dreher, J. Tarter, L. Blitz, M. Davis, M. Fleming, D. Bock, G. Bower, J. Lugten, G. Keleta, L. DâAddario, G. Harp, R. Ackermann, S. Weinreb, G. Engargiola, D. Thornton, and N. Wadefalk, "The Allen telescope array," *Proceedings of the SPIE*, vol. 5489, pp. 1021–1028, 2004.

[7] P. Hall, "The Square Kilometer Array: An Engineering Perspective," *Springer*, vol. 1st ed.

[8] F. J. Lockman, "The Green Bank Telescope: an Overview," *GBT Memo No. 192*, 1998.

[9] C. Salter, "An Astronomer's Guide to the Arecibo 305-m Telescope," *NAIC Memo*, February 2012.

[10] Netherlands Institute for Radio Astronomy, "ASTRON Home Page," http://www.astron.nl, [Online].

[11] Commonwealth Scientific and Industrial Research Organization, "CSIRO ASKAP Home Page," http://www.csiro.au/science/ASKAP, [Online].

[12] C. J. Jin, R. D. Nan, and H. Q. Gan, "The fast telescope and its possible contribution to high precision astrometry." *A Giant Step: from Milli- to Micro-arcsecond Astrometry, Proceedings of the International Astronomical Union, IAU Symposium*, vol. 248, pp. 178–181, July 2008.

[13] Collaboration for Astronomical Signal Processing and Electronics Research, "CASPER Home Page," https://casper.berkeley.edu/, [Online].

[14] "IEEE Standard Definitions of Terms for Antennas," *IEEE Std 145-1993*, p. i, 1993.

[15] K. Warnick, B. Jeffs, J. Landon, J. Waldron, D. Jones, J. Fisher, and R. Norrod, "Phased array antenna design and characterization for next-generation radio telescopes," in *Antenna Technology, 2009. iWAT 2009. IEEE International Workshop on*, march 2009, pp. 1 –4.

[16] B. Van Veen and K. Buckley, "Beamforming: a versatile approach to spatial filtering," *ASSP Magazine, IEEE*, vol. 5, no. 2, pp. 4 –24, april 1988.

[17] J. R. Nagel, "A prototype platform for array feed development," , Brigham Young University, , December 2006.

[18] J. C. Landon, "Development of an experimental phased array feed system and algorithms for radio astronomy," Ph.D. dissertation, Brigham Young University, April 2011.

[19] CASPER ROACH Documentation, "ROACH Home Page," https://casper.berkeley.edu/wiki/ROACH, [Online].

[20] CASPER x64ADC Documentation, "x64ADC Home Page," https://casper.berkeley.edu/wiki/X64_adc, [Online].

[21] CASPER PFB Documentation, "Polyphase Filter Bank Home Page," https://casper.berkeley.edu/wiki/Polyphase_Filter_Bank, [Online].

[22] CASPER FFT Documentation, "FFT Biplex Real Home Page," https://casper.berkeley.edu/wiki/Fft_biplex_real_2x, [Online].

[23] CASPER Medicina Correlator Documentation, "Medicina Correlator Home Page," https://casper.berkeley.edu/wiki/Medicina_Correlator, [Online].